Check for updates

MICROROBOTS

Si chiplet–controlled 3D modular microrobots with smart communication in natural aqueous environments

Yeji Lee[1,2], Vineeth K. Bandari[1,2]*, John S. McCaskill[1,2,3]*, Pranathi Adluri[1,2], Daniil Karnaushenko[1,2], Dmitriy D. Karnaushenko[1,2], Oliver G. Schmidt[1,2,3]*

Copyright © 2025 The Authors, some rights reserved; exclusive licensee American Association for the Advancement of Science. No claim to original U.S. Government Works

Modular microrobotics can potentially address many information-intensive microtasks in medicine, manufacturing, and the environment. However, surface area has limited the natural powering, communication, functional integration, and self-assembly of smart mass-fabricated modular robotic devices at small scales. We demonstrate the integrated self-folding and self-rolling of functionalized patterned interior and exterior membrane surfaces resulting in programmable, self-assembling, intercommunicating, and self-locomoting micromodules (smartlets ≤ 1 cubic millimeter) with interior chambers for onboard buoyancy control. The microrobotic divers, with 360° solar harvesting rolls, functioned with sufficient ambient power for communication and programmed locomotion in water via electrolysis. The interior folding faces carried rigid microcomponents, including silicon chiplets (Si chiplets) as microprocessors and micro–light-emitting diodes (LEDs) for communication. The exterior faces were able to engage in specific patterned docking interactions between smartlets. The heterogeneous integration is mass producible and affordable through two-dimensional (2D)–automated lithography and microchiplet bump-bonding processes, here shown to be compatible with subsequent autonomous 3D folding and rolling. The robotic modules functioned in natural aqueous environments, and the technology was analyzed as scalable down to microscopic dimensions. Selectively addressed communication with individual smartlets was enhanced via frequency-specific optical signals and enabled precise control, allowing each smartlet to be activated independently within a collective system. The work remodels modular microrobotics closer to the surface-rich modular autonomy of biological cells and provides an economical platform for microscopic applications.

INTRODUCTION

Mainstream microrobotics has long operated without powerful unplugged electronic control on sub–cubic millimeter scales because of surface area constraints on power, communication, memory, and logic. Information processing in microscopic robotics is still vastly inferior to that in living organisms. The three-dimensional (3D) folding of proteins and thin membranes into modular architectures enables a dense integration of mass-fabricated autotrophic and autonomous functions on accessible surfaces within cellular life (*1*). Functionally, this 3D deployment of self-folded, component-rich, active surfaces, capable of selectively interacting internally or with the environment, far surpasses the capabilities of monolithic chip technology, despite progress in the construction of onboard electronically controlled microrobots (*2*). Modular microrobotics requires the integration of natural power harvesting and storage, complex electronic control, sensors, and actuators beyond current levels of onboard control, especially in soft robotics (*3*–*7*). Heterogeneous integration without self-folding (*8*, *9*) has enabled progress in smart dust (*10*, *11*) and autonomous chiplets in solution (*12*, *13*), easing but not overcoming (*14*) the planar layering of massively parallel lithography (*15*) that has constrained progress in microrobotics.

Autonomous microrobots functioning at the sub-millimeter scale hold potential for transformative applications across environmental, medical, and industrial domains. The advanced forms of core robotic functions needed for such autonomous modular microrobots include ambient power harvesting (to allow prolonged activity in natural environments), self- and environmental sensing (to inform relevant actions), onboard electronic programming and control (to facilitate autonomous behavior), wireless intermodule communication (to coordinate collective behavior), and low-power electronically controlled microrobotic locomotion (to facilitate mobility, collective dynamics, and reconfiguration) (*16*). Previous studies have successfully implemented individual aspects of microrobotic functionality, such as actuation, energy harvesting, sensing, or communication, with key steps toward onboard electronic control taken in the development of sub-millimeter smart dust (*17*–*19*) and microscopic smart electrochemical lablets (*13*, *20*) based on complementary metal-oxide semiconductor (CMOS) chiplets, including early demonstrations of onboard microcontrol (*2*). However, the complete set of functionalities above—enabling fully untethered operation, independent programming, and modular reconfigurability—has rarely been integrated together in microscale robotic platforms to date. Micro-origami folding techniques (*21*–*23*) and Swiss-rolled structures (*3*, *14*) have enabled the conversion of structured membranes carrying electronic components and circuits into functional microstructures. These techniques have been used to fabricate passive freestanding (*24*, *25*), electronically active (*23*, *26*), and untethered microgrippers (*27*), as well as surface-tethered microrobots (*28*). Nevertheless, the power budget has continued to limit the capabilities of autonomous microsystems, despite substantial advances in the microscale integration of radio frequency (*29*), optical (*30*), and ultrasound (*31*) energy harvesting. Moreover, electronic actuators (*32*), sensors (*33*), and transistor microelectronics compete for the limited available power and space at these scales. Without full 3D integration—including interior surfaces enabled by self-folding—there is insufficient surface area at the ≤1-mm scale for either multifaceted docking (for

[1]Material Systems for Nanoelectronics, Chemnitz University of Technology, 09107 Chemnitz, Germany. [2]Research Center for Materials, Architectures and Integration of Nanomembranes (MAIN), Chemnitz University of Technology, 09126 Chemnitz, Germany. [3]European Centre for Living Technology (ECLT), Ca' Bottacin, Dorsoduro 3911, Venice 30123, Italy.
*Corresponding author. Email: vineeth-kumar.bandari@etit.tu-chemnitz.de (V.K.B.); john.mccaskill@main.tu-chemnitz.de (J.S.M.); oliver.schmidt@main.tu-chemnitz.de (O.G.S.)

Downloaded from https://www.science.org at The Hong Kong University of Science and Technology (Guangzhou) on May 25, 2026

self-assembly) or directional interrobot communication (for collective behavior).

Here, we realize a mass-fabricable, autonomous, and programmable modular microrobotics platform, extending the joint power of monolithic lithography and parallel heterogeneous integration via biomimetic self-folding fully into three dimensions. We demonstrate the simultaneous integration of modular self-assembly with the five key robotic functions—energy, sensing, control, communication, and actuation—realizing autonomous microrobots envisioned as smartlets in (*16*). The introduced smartlets are aquatic divers in three dimensions, are autonomous unlike the famous Cartesian diver known since Galileo's time, and exemplify this advancement. Self-folding of micro-origami membranes converts planar films into pentafunctionalized microrobots with accessible interior structures for functionalization. The folding faces carry rigid microcomponents including silicon chiplets used as microprocessors and micro–light-emitting diodes (μ-LEDs) for communication. The smartlets, with omnidirectional 360° solar harvesting, generate sufficient ambient power for locomotion in natural (e.g., lake) water via electrolysis, operating fully untethered and autonomously.

RESULTS

Chiplet integration in 3D-folded modular microrobots

The compact access to energy was achieved in this work by a carefully optimized multilayer process orchestrating the sequential self-folding and self-rolling of thin-film surfaces, which placed strong demands on the integration flexibility of control electronics. Although thin-film transistors (TFTs) were a natural choice, their miniaturization still lags (*34*) far behind crystalline CMOSs, consuming too much power for complex robotic control (*35*). Single-crystal chiplet microcontrollers with microscopic dimensions were produced previously (*36*), but for use on folded micro-origami robots, there was still the major challenge of parallel reliable fine-pitched electrical connection to thin conducting traces, which must robustly cross folds of their thin supporting surfaces. Here, we advanced the flip-chip bonding of microscale Si-CMOS chiplets and other microelectronic devices (down to the 100-μm scale) to such thin films, not only standard metallized polyimide (typically ≤5 μm thick) but also more complex multilayer films, including hydrogels required for micro-origami (*22*, *23*), allowing such devices to be deployed as rigid islands on the flexible faces of the micro-origami cubes, as shown in Fig. 1, independently of the rolled structures on the edges used for solar harvesting.

The integration of microelectronic sensors, actuators, and optical communication elements alongside planar bonded chiplets on thin films using sequential microrolling (*3*, *14*) and micro-origami self-assembly (*23*) techniques resulted in a compact multifunctional smartlet, including an omnidirectional solar power source, without compromising functionality. The detailed fabrication sequence is illustrated in Fig. 1A (see Materials and Methods for details). The process began with the creation of a soft polymeric body, forming the structural foundation (see Fig. 1B), followed by the deposition of the gold (Au) interconnect layer to establish electrical connectivity. Next, bubble-generating electrodes (BGEs) were fabricated through the sequential deposition of platinum (Pt) and nickel (Ni), forming electrochemical reactive elements (Fig. 1C). The intermediate fabrication steps for micro–organic solar cells (μ-OSCs) and micro–organic photodiodes (μ-OPDs) involved the sequential deposition of the anode, electron transport layer (ETL), photoactive polymer, hole transport layer (HTL), and Au contact layer, ensuring efficient energy harvesting and sensing capabilities. Copper/tin (Cu/Sn) bumps were then formed to establish interconnects for subsequent chiplet bonding. The process continued with the bonding of μ-LEDs and silicon microchiplets (μ-chips), integrating optical communication and computational elements (Fig. 1D). Selective (SU-8) polymer passivation was applied to the rigid faces to provide electrical insulation while maintaining flexibility (Fig. 1E). The μ-OSCs were then self-rolled to align them for omnidirectional energy harvesting, and last, the structure was reliably assembled in three dimensions, transforming it into a compact cube adorned with eight tubes on its eight edges, as illustrated in Fig. 1 (A to G) (see movies S1 and S2). Five functional components enabling autonomous robot functionality, visible at different orientations of the smartlet cube in Fig. 1F, were integrated (also quantified in Fig. 1G): omnidirectional energy harvesting by μ-OSCs; orientation-sensing by μ-OPDs; a custom programmable silicon CMOS chiplet (μ-chip) (*12*, *13*), controlling the smartlet on board; μ-LEDs in different colors enabling optical communication between smartlets; and BGEs splitting water into gas bubbles (hydrogen H_2 and oxygen O_2) within the cube, enabling reversible buoyancy modulation governed by the μ-chip program. All of the external faces of the smartlet cube were unoccupied, allowing them to be used for modular self-assembly control. The mass fabrication resulted in cut tapes of many smartlets (Fig. 1H).

Compact rolled surfaces for omnidirectional ambient solar powering

Naturally occurring unconcentrated sunlight is limited to 1 mW/mm^2 (1 sun) and should ideally be captured at all microrobot orientations. The poly(3-hexylthiophene) and-phenyl-C_{61}-butyric acid methyl ester (P3HT:PC_{61}BM) μ-OSCs used here were flexible, integrable, and theoretically capable of 33% power conversion efficiency (PCE) (*37*). By integrating these materials onto prestrained polymeric films, we created self-rolled microtubes whose performance was independent of altitude light angle upon release (see Fig. 2 and fig. S1). A single rolled μ-OSC could generate a PCE up to 11.5% at a short-circuit current (I_{sc}) of 50 μA and an open-circuit voltage (V_{oc}) of 0.65 V. Strategically positioning eight rolled μ-OSCs along the eight edges of the smartlet and connecting them in series allowed for omnidirectional energy harvesting and increased the output voltage (Fig. 2A) while keeping the smartlet faces available for microelectronic integration. To evaluate the structural transformation on energy harvesting, we first measured the performance of the μ-OSCs in a planar state using a 3D light dome to analyze the dependence of power generation on the incident light angle (Fig. 2B). The results showed changes in PCE as the illumination angle varied, indicating sensitivity to directional light exposure (Fig. 2C). In contrast, after self-assembly into the 3D smartlet architecture (Fig. 2D), the power output became angle independent, confirming that the unique spatial distribution of μ-OSCs along the smartlet's edges enabled uniform energy harvesting irrespective of incident light direction (Fig. 2, E and F). This structural adaptation ensured consistent and stable power supply, optimizing the energy efficiency of the smartlet across diverse environmental conditions. In addition, this design achieved a maximum PCE of

Downloaded from https://www.science.org at The Hong Kong University of Science and Technology (Guangzhou) on May 25, 2026

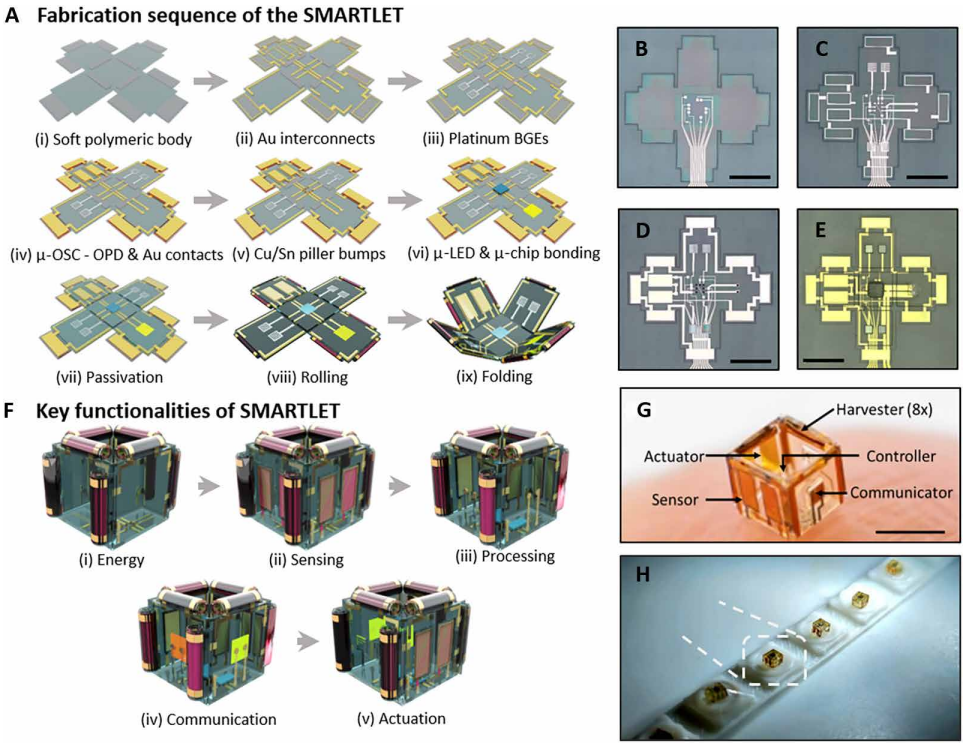

Fig. 1. Functional integration of programmable modular robotic cubes (smartlets). (**A**) Schematic illustration of the fabrication sequence of the smartlet. Steps: (i) creation of soft polymeric body; (ii) Au interconnect layer; (iii) deposition of Pt and Ni for BGEs; (iv) intermediate steps for μ-OSC and μ-OPD fabrication, including anode, electron transport layer, photoactive polymer, HTL, and Au contact layer; (v) preparation of Cu/Sn bumps; (vi) bonding of μ-LEDs and silicon μ-chips; (vii) selective SU-8 polymer passivation on rigid faces; (viii) rolling μ-OSCs; and last (ix) folding self-assembly of faces into the cube. (**B**) Patterned carrier layer (polyimide) and metal traces (Au) with faces of the cube flanked on all eight exterior edges by beveled rectangles for the μ-OSCs (scale bar, 1 mm). (**C**) Additional patterned Au interconnect layer with BGEs deposited on the top and bottom faces of the cube (scale bar, 1 mm). (**D**) Patterned μ-OSC, μ-OPD, and Cu/Sn pillar bumps formed for the subsequent bonding process (scale bar, 1 mm). (**E**) Planar smartlet after bonding of μ-LEDs and μ-chips followed by passivation (scale bar, 1 mm). (**F**) Computer-aided design (CAD) rendering of the assembled smartlet with the key successive functionalities in this work, shown in the relevant cube orientations. (**G**) Multifunctional, programmable micro-origami cube, resting on a fingertip, integrated with an eightfold μ-OSC energy harvester for power, μ-OPDs as sensors for use as orientation detectors and as communication receivers, a pulsed μ-LED as a sender for optical communication, BGEs operating via a photoelectrochemical mechanism as actuators, and a μ-chip with 180-nm-resolution CMOS transistors as the onboard controller for programming and control (scale bar, 1 mm). (**H**) Linear tape containing smartlets fabricated photolithographically and self-assembled in parallel, apart from the now semiautomated pilot serial chiplet and LED bonding process, which, being planar, scales efficiently like LED assembly down to microscopic dimensions.

up to 3.75% in optimized smartlets without bypass diodes, with an average output of $I_{sc} = 7$ μA and $V_{oc} = 2.1$ V and an approximate maximum up to 37.5 μW in the best smartlets. This energy was sufficient to power all functionalities of the smartlet simultaneously in this work.

Awareness of orientation is important for smartlets for docking or navigation. The two μ-OPDs mounted on one face of the cube (Fig. 2G) exhibited systematic voltage variation in response to changed orientation or distance of incident light (e.g., from other smartlets or the 1-sun source). μ-OPDs on multiple faces (fig. S2) could measure a wider range of orientations simultaneously, as shown in Fig. 2H. Additional detector faces readily available on docked modules, controlled orthogonal self-rotation, or additional reference beams from fixed smartlets may be used in the future to sense full 3D orientation.

Onboard programming with peer-to-peer communication by light

The integration of CMOS chiplets into fold-up smartlets delivered powerful onboard microcontrol, elevating soft folded 3D thin films to complex programmable microrobots. In Fig. 3, we demonstrated this programmability in connection with optical communication between smartlets. Communication between smartlets is needed to enable them to coordinate actions, share critical information, or collectively tackle complex tasks. As opposed to single binary or analog signals, which could be realized physically in simpler interacting systems, peer-to-peer communication of highly specific binary encoded commands and whole programs, as demonstrated here, was unprecedented at this scale, opening the potential for sophisticated programmed collective dynamics in the future. Optical communication, although attractive in high speed, large bandwidth, minimal interference, and low signal attenuation and successfully miniaturized (*30*), had been hitherto limited in microrobotics by the power needed for optical transmission. Two programmable chiplets were used here: the lablet microprocessor chiplet (*12, 13*), designed to deliver complex temporal signal patterns to multiple electrodes for electrochemical and electrokinetic manipulation (μ-chip1 in Fig. 3, A and B), and a commercial LED driver chiplet (*38*), useful for the higher currents of green LEDs and larger actuators (μ-chip2 in Fig. 3, C and D). In both cases, serial programs were loaded bitwise and stored in shift registers to digitally control the temporal sequence of driving voltages on several actuator pads as demonstrated in Fig. 3 (B and D).

Two pairs of μ-OPDs and two μ-LEDs were mounted on four faces of the smartlet in Fig. 3E. The green transmitter and red indicator LEDs, addressed by the μ-chips shown in Fig. 3 (F and G), could be used not only to visualize the internal actuation generated by the μ-chip program but also to send data or commands from one smartlet to the next (movie S3). The two photosensors on each face, connected in series, generated a signal of 1 to 1.2 V usable as a pulsed digital input to the μ-chip data input channel, decoded as a command or program for the chiplet. In Fig. 3H, the green LED on a single smartlet was capable of transmitting data at rates from 1 to 1000 Hz, conveying digital information to a second smartlet through the aqueous medium at separation distances under 4 mm without physical contact. The external electrical connections were selectively used for calibration, verification, and component-level testing. The separation distance would be sufficient to support local communication

Downloaded from https://www.science.org at The Hong Kong University of Science and Technology (Guangzhou) on May 25, 2026

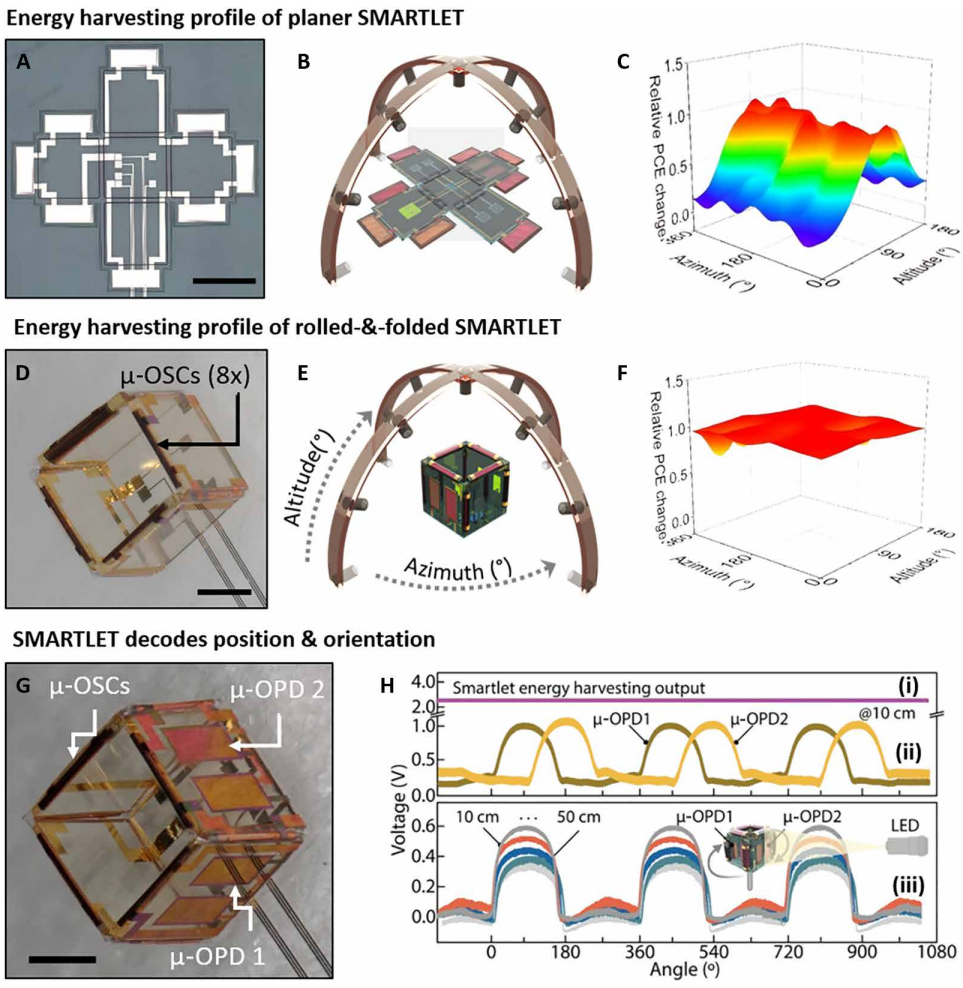

Fig. 2. Self-powering and sensing functionality of smartlets. In this figure, the smartlets are tethered with connecting wires [visible in (A), (D), and (G)] to external circuits, merely to allow electrical performance calibrations. (**A**) Eight planar patterned μ-OSCs connected in series (scale bar, 1 mm). (**B** and **C**) Schematic measurement setups (B) and surface plots (C) of the relative change in measured PCE of a smartlet as a function of incident light orientation (azimuth and altitude angles) in 3D in the prefolded state, for an illumination intensity of 50 μW/cm^2. (**D**) Self-assembled smartlet with eight rolled μ-OSCs (scale bar, 0.5 mm). (**E** and **F**) Schematic measurement setups (E) and surface plots (F) of the measured relative change in PCE of a smartlet as a function of incident light orientation (azimuth and altitude angles) in 3D in the postfolded state, for an illumination intensity of 50 μW cm^{-2}. (**G**) Smartlet with rolled μ-OSCs and μ-OPDs (scale bar, 0.5 mm). (**H**) (i) Orientation independence of solar harvesting (purple) for the entire smartlet (eight deployed μ-OSCs), (ii) contrasted with orientation-sensitive orthogonally directed photodetectors μ-OPD1 (brown) and μ-OPD2 (yellow) as the smartlet continuously rotates around its symmetry axis. (iii) μ-OPD response as a function of angle is measured for three full rotations at five distances, with the schematic inset showing orientation axes.

during docking or in swarms of smartlets in future work. Figure 3 (I to K) demonstrates the practical communication between smartlets of functional information such as start and stop commands. On the receiving smartlet (R_x), its programmed red-light pulses were started and stopped by commands encoded as green light from the sending smartlet (T_x) (movie S4).

Power sufficiency for overall functionality

The rolled μ-OSCs integrated into the smartlet generated a maximum power of up to 37.5 μW under standard illumination conditions (1 sun, 100 mW/cm^2). This power was distributed to support the following functionalities: μ-LEDs for optical communication, consuming ~1 μW (green) and 1.5 μW (red); the CMOS chiplet for logic operations and receipt of (photo)sensor signals, operating in two modes—sleep mode (0.16 to 0.25 μW) and active mode (4.0 to 6.3 μW)—depending on processing demands; and BGEs for propulsion, consuming 10 to 25 μW during operation. The total onboard power consumption therefore ranged from 16 μW during low-demand operation to ~33 μW during high-demand operation. This analysis demonstrated that the energy generated by the μ-OSCs was sufficient to power the system even during peak operational states. Underpowering the BGEs caused the voltage to drop only to the threshold voltage required for electrolysis, a voltage that, at ≥1 V, was sufficient to support the other smartlet functionalities, so that although actuation was slowed, other functions remained intact. For example, with one-third lower solar power, allowing operation at greater depths or in water with natural sediments (see Discussion), the limiting available power to BGEs was still 15 μW, and the only effect on robot operation was to slow buoyancy changes down to two-thirds of the maximum duty cycle. Furthermore, the smartlets used duty cycling for the CMOS chiplet, μ-LEDs, and BGEs, ensuring that energy-intensive operations were only activated when necessary, minimizing power waste and sustaining continuous functionality under solar illumination.

Intercommunicating onboard control of microrobotic aquatic divers

We addressed the onboard robotic motion control of smartlets in an ensemble in Fig. 4. Although external actuation is useful in some scenarios, independent agents would require the more challenging control and powering autonomy of onboard actuation—beyond external magnetic fields (*39*) or light (*2*) controlling individual locomoting microrobots. Full power autonomy requires replenishable onboard resources, unlike metallic catalytic motors (*14*, *40*). The chosen actuator mechanism was one that only required water and should be applicable in many natural environments, using μ-OSCs in series to create an electric potential sufficient to split water. To ensure efficient electrochemical actuation, we used Ni and Pt coatings to catalyze the oxygen and hydrogen evolution reactions, respectively, as illustrated in Fig. 4A. Successful integration of such bubble BGEs into the smartlet is shown in Fig. 4 (B to D), in action together with μ-OSCs under 1-sun illumination (movie S5), and then in combination with the other

Downloaded from https://www.science.org at The Hong Kong University of Science and Technology (Guangzhou) on May 25, 2026

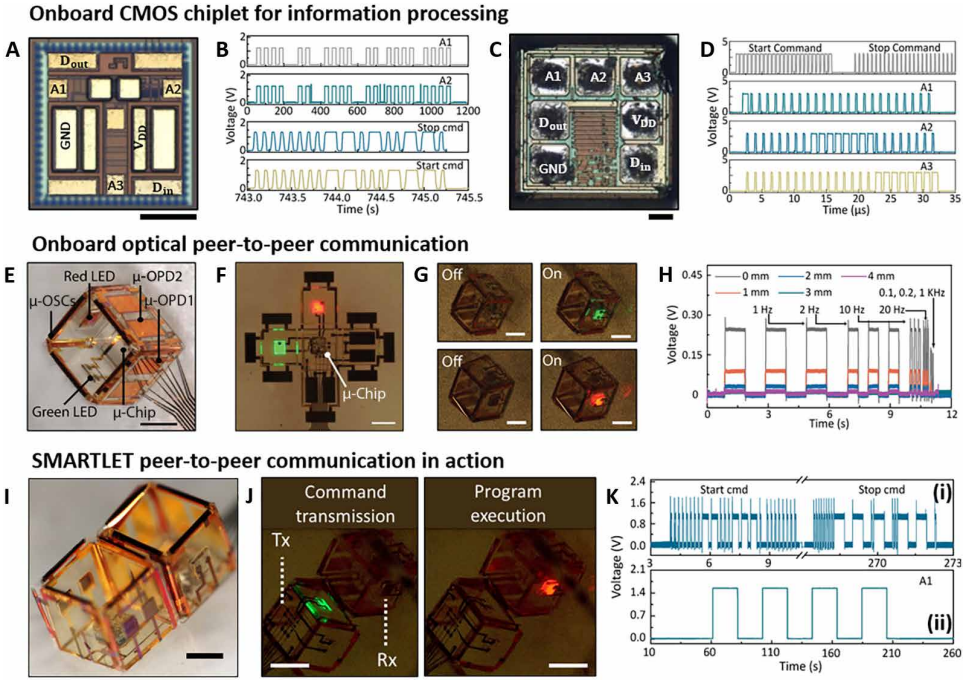

Fig. 3. Smartlet onboard digital logic and optical communication. (**A**) Microscope image of μ-chip1, a custom microcontroller CMOS chiplet, 140 μm by 140 μm by 50 μm, displaying the input/output (in/out) interfaces used here: actuator outputs A1 to A3, program input D_{in} and output D_{out}, ground GND, and power supply V_{DD} (scale bar, 50 μm). (**B**) Programming and output waveforms of μ-chip1 after bonding to a flexible substrate with Cu/Sn pillar bumps. (**C**) Microscopic image of μ-chip2, a three-color (24-bit) LED driver chiplet WS2812B43, 300 μm by 300 μm by 100 μm, displaying all of the in/out interfaces A1 to A3, actuator outputs; D_{in} (receiving)/D_{out} (transmitting), program input and output; GND, ground; V_{DD}, supply input (scale bar, 50 um). (**D**) Programming and output waveforms of the driver chiplet after bonding. (**E**) Microscope image of the smartlet, integrated with μ-OSCs, μ-OPDs (μ-OPD1 positioned on the lower face and μ-OPD2 positioned on the right face), μ-chip, and green and red μ-LEDs positioned on the left and upper faces (scale bar, 0.5 mm). (**F** and **G**) Microscope image of the before (F) and after (G) self-assembly smartlet displaying LEDs controlled by μ-chip: green (transmitter connected to D_{out} of μ-chip2) and red (indicator connected to A1 of μ-chip1 or μ-chip2) (scale bar, 0.5 mm) (see movie S3). External electrical connections were selectively used for calibration, verification, and component-level testing. (**H**) Intersmartlet communication: operating bandwidth and distance characterization of the μ-OPD photosensors' response to a green light–transmitting smartlet at 0 to 4 mm. (**I** to **K**) Two optically communicating smartlets: (I) microscope bright image (scale bar, 0.5 mm). (J) Low-light images of transmitting (T_x green) and receiving (R_x red) smartlets in three steps: T_x sending the start command, R_x execution of its program, T_x sending the stop command (see movie S4) (scale bar, 1 mm). (K) (i) Optical start and stop commands as specific pulse sequences generated by reception of programmed light directed at the μ-chip and (ii) actuation signal (A3) initiated (activated) by the start command and stopped by the stop command.

functional components, before and after self-folding, in Fig. 4 (C and D), respectively.

Directed intersmartlet local light programming, as depicted in Fig. 4E, represented an advance in actuation control for modular robotics at this scale. Smartlet programs on the attached lablet μ-chip were 58 bits in length and encoded a state machine that had four operating states (idle, programming, running, and sending) and was sensitive to external eight-bit commands while idle or running. Figure 4 (F and G) shows the ensuing locomotion, with one smartlet (S2) optically transmitting a command, "start your locomotion program," to a second smartlet (S3) in the presence of a third (S1). This program initiation triggered a series of actions in the programmed smartlet S3. The smartlet began generating bubbles inside, and once a critical gas volume accumulated, the smartlet levitated, free to rotate and laterally translate, propelling upward. After reaching the surface, the onboard program halted the bubble generation, and the remaining bubbles started to dissolve (*41*), reducing smartlet buoyancy and causing it to return to the vessel floor (fig. S3 and movie S6). This controlled movement, with timed surfacing cycles, demonstrated the potential for sophisticated motion control enabled by the programmable μ-chip.

Figure 5 shows both the selective-in-ensemble and local communication needed for modular robotics. First, different digital identifications (IDs) and communication frequencies of variant CMOS chiplets enabled the selective global addressing and hence motion control of individual smartlets within a collective, as demonstrated in Fig. 5 (A and B), where smartlets S2 and S3 were untethered but responded to programs and commands issued at different data transmission rates. Only smartlet S3 was programmed in response to the global 200-Hz light-encoded command: It ascended to the surface, where it stayed for some time. Whereas the large excess buoyancy of S3 slowly depleted via bubble solvation, smartlet S2 was programmed to navigate repetitively to the surface and back to the floor twice, with a smaller excess buoyancy, before receiving a 50-Hz encoded stop command and returning permanently to the floor (fig. S4 and movie S7). Overall, local (intersmartlet) and global light commands, both demonstrated for smartlets, provided programmable functions for coordinating and controlling collective movement (*42*). It is expeditious to separate this initial advance from the extensive follow-on work needed to exploit the rich collective behavior in larger numbers of smartlets.

Self-assembly of smartlet modules

Active modular robots were previously shown to assemble into larger structures by controlled docking at centimeter scales (*4*, *43*). Although the self-assembly of passive modules via hydrophobic-hydrophilic patterning (*44*, *45*)—in the form of millimeter-scale disks (*44*), magnetic barcode patterning (*46*), or specific DNA hybridization on gel cubes (*47*)—had been demonstrated, often with the option of environmentally switchable docking interactions, these methods typically required mechanical agitation at sizes where inertial forces dominated over Brownian motion ($\gtrsim$1 μm). Nevertheless, active, self-locomotion–assisted assembly for microrobots at or below the 1-mm scale remained largely unexplored. Here, we demonstrated the dynamic interplay between long-range, locally programmed smartlet self-locomotion and short-range self-assembly, as shown in the sequence of still frames in Fig. 5 (C and D), with full video documentation in movie S7. Smartlets autonomously navigated to the

Downloaded from https://www.science.org at The Hong Kong University of Science and Technology (Guangzhou) on May 25, 2026

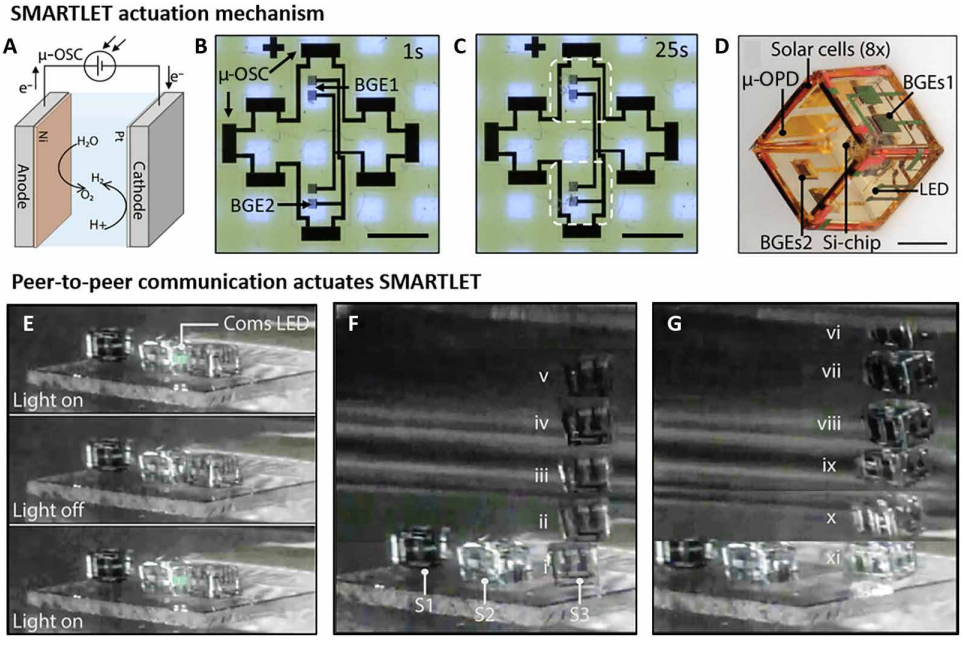

Fig. 4. Programmed locomotion in water via onboard digital logic. (**A**) Schematic of the working mechanism of electrochemical water splitting into H_2 and O_2 gas bubbles at Pt- and Ni-coated electrodes. (**B** and **C**) Microscope images showing bubble generation at two integrated electrochemical BGE pairs (the Pt and Ni electrodes) powered by μ-OSC solar cells under standard solar illumination (1 sun) in an unfolded smartlet (scale bar, 1 mm). (B) and (C) show the process at 1 and 25 s, respectively. For the full time sequence, see movie S5 (in medical saline, an example of a natural medium for medical applications). (**D**) Microscope close-up of the smartlet, after self-assembly, showing organic solar cells, photodiodes on the left side, a microchip at the center, LEDs on the right side, and electrochemical BGEs on both the upper and lower faces of the cube (scale bar, 0.5 mm). (**E**) Snapshots demonstrating three frames (on-off-on) taken from active smartlet communication via green μ-LED on the transmitting smartlet (T_x) to the receiving smartlet (R_x) μ-OPD sensor. (**F** and **G**) Real-time image overlay sequence illustrating how electrochemical buoyancy engines via BGEs, switched on and off by the onboard program, cause the smartlet S3 to move first up (i to v) (F) and then down (vi to xi) (G). In this case, the tethered smartlet S2 sends the start command via its green μ-LED [as shown in (E)] to initiate the autonomous programmed locomotion sequence up and down repeatedly with intermissions on smartlet S3. For the full time sequence, see movie S6 (performed in filtered natural lake water).

liquid-air interface under onboard electronic program control. Once buoyant, they were laterally attracted to each other via surface tension forces acting on their displacement menisci, enabling them to approach and dock. Depending on the programmed individual or synchronized diving behavior—through controlled deactivation of their bubble generators at either staggered or synchronized timings—smartlets could either undock on command (Fig. 5C, xii) or return to the beaker floor. This work therefore represented a rare demonstration at the 1-mm scale of electronically controlled, self-locomotion–enhanced self-assembly of modular robots. All smartlet demonstrations—locomotion, docking, and peer-to-peer optical communication—were performed fully untethered and powered by onboard omnidirectional solar harvesting.

The self-assembly of such multifunctional robotic smartlets could also be made face specific. Through specific hydrophobic-hydrophilic 2D-barcode subpatterning of the outer faces of the smartlet, face-selective self-assembly based on matching surface patterns and self-locomotion was achieved at the 1-mm scale for fully functional electronic robot modules (see Fig. 5, E to I). The exclusive use of inner faces of smartlet cubes for functional elements, with light harvesting relegated to edge rolls, left the outer faces available to control docking as shown schematically in Fig. 5 (E to G). However, these surfaces, which faced down toward the sacrificial layer (SL) during micro-origami fabrication, are not straightforward to pattern hydrophobically. We used e-beam–deposited molybdenum trioxide (MoO_3) structured by lift-off as a water-soluble SL for a special precursor layer, which only later became hydrophobic after heat treatment. These patterns were masked via planar lithography, maintaining the mass-producible nature of the assembled smartlet robotic modules (see Materials and Methods for details).

Smartlets self-assembled into specific modular structures, with docking of matching cube faces, when placed in the vicinity of one another. The autonomous long-range transport required to bring appropriate aquatic divers to such vicinity, in the absence of macroscopic agitation (*44*–*47*), was demonstrated above (Fig. 5C). Examples of assembled multimodule structures are shown in Fig. 5 (H and I). They were held together by the standard hydrophobic/hydrophilic patterned forces for self-assembly in water (*45*). Smartlets first self-assembled to primitive shapes, like short linear chains or square arrays. To emulate the long-range transport recycling of additional smartlets in global self-assembly, considering the slow diving cycles of the current smartlets, we simply added them manually into the vicinity, where they self-assembled onto the above assemblies. Both completely face-registered (Fig. 5H) and half-offset (Fig. 5I) self-assembled structures were achieved through the design of the surface tension controlling patterns to include peripheral rectangular registration guiding elements (see Fig. 5E).

DISCUSSION

This integration of autonomous natural powering and onboard electronic control of locomotion and intermodule communication takes peer-to-peer microrobotic control beyond simpler physicochemical mechanisms (*48*). Although our robot demonstrations are simple, the pathway is now wide open to engineer, with incremental design, improvements to functionality and further miniaturization. A chiplet tuned for modular microrobotics, with enhanced functionalities and the memory of a current CMOS, will soon extend the binary sensor feedback control in lablets to the higher temporal and signal strength resolution required for complex robotic action. The bonding of chiplets onto the in-folding surfaces allows a large increase in functional surface area inside microrobots, freeing exterior surfaces for multimodule docking interactions both by self-assembly and active locomotion. Internal buoyancy control has already proven to be an efficient mechanism of powering underwater gliding locomotion

Downloaded from https://www.science.org at The Hong Kong University of Science and Technology (Guangzhou) on May 25, 2026

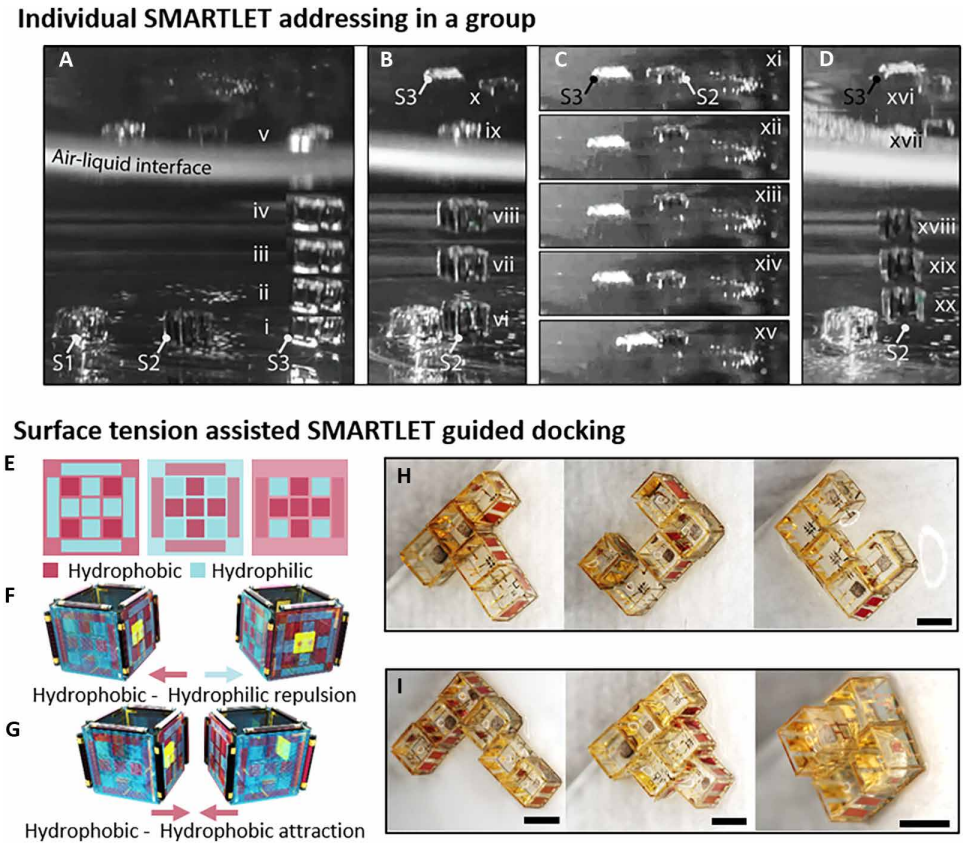

Fig. 5. Smartlet collective motion and guided self-assembly. (**A** and **B**) Real-time image overlay sequence depicting frequency-selective, individually instructed smartlets S3 and S2, both untethered, commencing locomotion programs selectively in response to command data: (A) S3 sent at 200 Hz (i to v) and (B) S2 at 50 Hz (vi to x). (**C** and **D**) Autonomous active docking and undocking of two smartlets assisted by surface tension. (B) The second smartlet, S2, locomotes from the glass beaker bottom to the air-water interface with excess buoyancy under the control of its onboard program (overlaid frames vi to x), near to where the first smartlet, S3, has already arrived. Smartlet S1 provides a stationary point of reference. (C) After initial kinetic repulsion (xi and xii) and then capillary attraction (xiii and xiv), the two smartlets dock together (xv) with the assistance of surface tension. (D) Under the active control of its onboard program, smartlet S2 ceases bubble formation, reducing its buoyancy to overcome the surface tension forces holding it to smartlet S3, and returns to the beaker bottom (xvi to xx). For the full time sequence, see movie S7 (in lake water as in movie S6). (**E**) 3D CAD drawings of the hydrophobic-hydrophilic patterning of the outer surfaces of the smartlet cubes. (**F** and **G**) Repulsion of nonmatching and attraction of matching patterned smartlet faces in water. (**H** and **I**) Partially guided self-assembly of smartlets: (H) into the letters "T," "U," and "C." Linear self-assembled primitives of two or three smartlets are brought together with laterally placed smartlets that dock by self-assembly to complete the structures. (I) Self-assembly of other structures, including half-registered contacts, enabled by the registration controlling rectangles (scale bar, 1 mm).

in ocean monitoring underwater drone vehicles (*49*). The onboard lablet programs already support multiactuator control (*13, 50*), making independent control of the two onboard bubble generators straightforward and permitting left-right locomotion control through tilt and hence 3D-controlled movement of smartlets equipped with gliding flaps.

The solar cells in the smartlets were fabricated using thin-film organic materials, with a total thickness of less than 5 μm before rolling (see fig. S5). The overall design of the smartlets was carefully optimized to balance energy harvesting, locomotion, and structural integrity. The rolled solar cell design ensures minimal interference with the hydrodynamic properties of the smartlet while providing sufficient power for untethered operation. Given their placement along the edges of the smartlet cube, each μ-OSC experienced differing levels of illumination depending on orientation, which can affect overall energy generation efficiency. The current design has been optimized to mitigate these effects through strategic placement of the μ-OSCs along the cube's edges. This configuration allows for multiangle light harvesting, as demonstrated in figs. S6 to S8, ensuring that at least a subset of the μ-OSCs remains illuminated under typical lighting conditions. Despite localized variations in power generation, the system can still supply sufficient energy to operate all onboard components, as detailed in Results. Figure S9 shows how the postfolding V_{oc} remains within the functional range, indicating that the system remains operational despite illumination differences. To further improve energy efficiency, we are exploring strategies such as integrating individual bypass diodes for each μ-OSC. This would prevent underperforming or shaded cells from limiting the performance of the entire serially connected circuit. A hybrid serial-parallel configuration could also be implemented to minimize voltage drops caused by shading effects, ensuring a more consistent power supply across all units, and we also envisage the integration of energy storage devices (supercapacitors and microbatteries) to further buffer fluctuations in light intensity. Although the current configuration maximizes photovoltaic integration without interfering with the self-folding hinges, we recognize that additional thin-film solar cells could be incorporated on previously unused surfaces in future designs. However, any such modifications would need to balance energy harvesting improvements with mechanical integrity, actuation, and docking functionalities.

The integration of 3D solar harvesting is the key step to ambient powered microrobotics in natural environments. We discuss the limitations to ambient power levels achieved and the influence of water quality on microrobot function. Unplugged (untethered without artificial power sources) near-surface operation in clear water was experimentally demonstrated, with operation in murky or deep water limited by light penetration, which is strongly wavelength dependent. Surface reflection at 90° incidence is only ~2%. Although 70% of solar energy is absorbed in the first 3 m, absorption loss is predominantly at wavelengths in ultraviolet (UV) and infrared (IR) that contribute little to powering the tubular solar cells (see fig. S10B). The μ-OSC absorption wavelength profile was chosen to match well with the low absorption window in water in the blue, so that harvested power losses in the first 10 m are <40% (see fig. S11). The rolled

Downloaded from https://www.science.org at The Hong Kong University of Science and Technology (Guangzhou) on May 25, 2026

solar harvesting collectors provide 50 to 100% excess power for key operations, permitting operation to depths of more than 1000 times the smartlet module size. To confirm operation in murky water, we conducted experiments measuring the performance of μ-OSCs submerged in pure Dulbecco's phosphate-buffered saline (DPBS) and in systematically contaminated DPBS (with 1 to 5% lake clay/mud, representing surface-level contamination down to ~10 m in depth). The results revealed that solar cell performance decreased by 60% at 5% (by weight) contamination (see fig. S11). These findings indicate that smartlets can generate sufficient power in environments with up to ~2 to 3% contamination or equivalent to depths of 5 to 10 m in a freshwater lake.

By conducting locomotion and assembly experiments in two application-relevant fluids with natural buffering capacity, we ensure that our results reflect the practical performance of the smartlets in diverse application scenarios. These results confirm that the electrolysis-based propulsion mechanism remains highly effective in both medical saline and naturally occurring freshwater environments, highlighting its versatility for diverse applications. The presence of impurities, including ions and organic molecules, in natural water can influence hydrophilic-hydrophobic interactions and the docking processes. Contaminants can alter the wettability of patterned regions. For instance, multivalent cations such as calcium ions (Ca^{2+}) and magnesium ions (Mg^{2+}) can form salt bridges between hydrophilic regions, and anions like chloride ion (Cl^-) or sulfate ion (SO_4^{2-}) may enhance the wetting of hydrophobic surfaces, increasing unspecific assembly (*51*–*53*). Surfactants, beyond the natural low concentrations found in clean lake water, were deliberately excluded from these experiments because of their known disruptive effects on hydrophobic-hydrophilic interactions (*54, 55*). Alternative patterning processes involving fluorocarbon patches, with binding orthogonal to both the hydrophilic and hydrophobic ends of natural amphiphiles, could later be used in more surfactant-rich natural environments if required and sustainably recoverable. Powering under varying daylight conditions, or in deeper or less transparent aqueous medium, will eventually require onboard power storage and intermittent robot operation, which are possible developments because of the advanced electronic control and achievement of interior chambers for batteries or supercapacitors. In addition, light scattering and absorption could interfere with optical communication, as could biofouling and contaminant deposition, which could affect both propulsion efficiency (*56, 57*) and docking mechanisms. Further assessments of system robustness to perturbation will be required, along with further enhancements in mobility control, en route to applications.

The smartlets use electrochemical actuation via BGEs, leveraging Ni and Pt catalysts for hydrogen and oxygen evolution, enabling untethered locomotion in aqueous environments. In contrast, phase-change actuators (*58, 59*) rely on thermal-driven transitions for buoyancy modulation, offering high-force output but requiring external heat sources or higher energy consumption, leading to delayed response times because of thermal inertia. Although effective for larger-scale soft robots, their scalability to the microscale is limited by thermal management and fabrication constraints. Electrochemical actuation, on the other hand, integrates seamlessly with thin-film deposition, microfabrication, and self-folding, ensuring chemical and thermal stability without additional material layers that could compromise the smartlets' delicate structure. An alternative potential solution to the steered buoyancy gliding introduced above, for achieving full 3D motion control, is to strategically position BGEs inside the eight tubular structures (which also house the solar cells) along the diagonal edges of the smartlet cube. These hybrid tubes, incorporating both solar cells for energy harvesting and BGEs for electrolysis-based propulsion, would function as microjet thrusters, like the double-jet microengines reported in (*3*). Because the bubble generators are then placed at orthogonal diagonal edges, activating specific sets of BGEs would enable controlled movement in the *X*, *Y*, and *Z* directions. Each such BGE tube consumes ~2.3 μW during operation, with locomotion along a single axis requiring multiple BGEs to thrust. Sustaining full 3D locomotion may require duty cycling strategies where movements are activated only when necessary to optimize energy consumption. The advantage of such an approach would be shorter reaction times for locomotion, at the expense of increased power compared with the buoyancy glider. These approaches could be combined. Future iterations may also incorporate onboard energy storage solutions, such as microsupercapacitors, to buffer energy for high-power maneuvers.

Another key challenge is enhanced environmental perception. The current system has limited sensing capabilities for detecting and responding to obstacles autonomously: It would have to rely on sensing changes to reflected LED light. Future designs could use freed-up faces of the cube to integrate advanced sensing technologies, such as a light detection and ranging (LIDAR)–like system, using orthogonal pairs of LEDs (consuming up to 5 μW) and photodiodes (consuming up to 1 μW) to enable real-time distance measurement and obstacle detection. Alternatively, piezoelectric materials (consuming ~0.5 to 5 μW in the frequency range from 10 kHz to 1 MHz), embedded within the smartlet structure, would facilitate sonar-based sensing, which is particularly effective in low-visibility or murky environments. By incorporating these navigation and sensing improvements, future smartlets could map their surroundings, detect obstacles in real time, and dynamically adjust their movement to navigate more effectively in complex environments.

This work demonstrates a system that combines independent energy harvesting, computation, locomotion, communication, and modular self-assembly—achieving a level of integration at the microscale that was rare in prior studies. Previous studies have successfully implemented individual aspects of microrobotic functionality, such as actuation, energy harvesting, sensing, or communication; however, systems that combine all of these elements into a single self-sufficient robotic platform at sub-millimeter scales remain extremely limited. The smartlets uniquely integrate omnidirectional energy harvesting via micro-organic solar cells, real-time environmental sensing through onboard photodetectors, onboard logic execution using a CMOS-based microchiplet, electrochemical locomotion via bubble generation, peer-to-peer communication enabled by frequency-selective optical signaling, and docking and self-assembly via hydrophobic and hydrophilic interactions. This combination of functionalities enables fully untethered operation, independent programming, and modular reconfigurability—capabilities that have not been demonstrated together in previous microscale robotic platforms.

The patterned self-assembly of smartlets relies on different hydrophobic-hydrophilic forces between matching and nonmatching docking faces. The magnitude of these forces on contact, in the 100- to 400-μN range (see Supplementary Methods: Detailed calculation of hydrophobic and hydrophilic interactions in self-assembly and motion at interfaces and table S1), is much larger than the buoyancy

Downloaded from https://www.science.org at The Hong Kong University of Science and Technology (Guangzhou) on May 25, 2026

forces in the range of 10 μN and drag forces in the <100-nN range. The strong adhesion for hydrophilic-hydrophilic docking ensures robust self-assembly even during buoyancy-induced movement. Smartlets are thus capable of stable self-assembly and reconfiguration in aqueous environments while maintaining independent movement and docking capabilities. When compared with other state-of-the-art microrobotic systems (*2*, *28*), which feature silicon-based CMOS integration for actuation and movement, smartlets are 3D modular robots, capable of real-time multiagent interaction and autonomous decision-making, and have free surfaces to engage in dynamic self-assembly. Unlike prior works that relied on artificial or concentrated external energy sources and/or external control (*60*–*63*), the smartlet platform achieves true ambient autonomy by integrating isotropic onboard energy harvesting with embedded digital logic circuits. Bandari *et al.* (*3*) have demonstrated flexible microsystems capable of controlled actuation via wireless power transfer, but these systems lacked digital control, peer-to-peer communication, or modular docking mechanisms—features that are crucial for autonomous modular microrobots.

The current work establishes individual microrobot control within an ensemble, using frequency-selective and pulse-encoded communication to enable smartlets to receive commands independently without global activation. This contrasts with mainstream magnetic, optical, or ultrasound microrobotics, which primarily relies on global control mechanisms rather than targeted, selective communication. In addition, our system demonstrates functional locomotion and docking in a 3D aquatic environment, expanding the range of potential applications beyond 2D microfabricated robots.

Conclusion: Scalability of the technology

As a modular, mass-producible platform (instead of modular, mass producible entity), smartlets are compatible with automated flip-chip bonding of chiplets, enabling rapid development cycles and parallel testing. Given these properties (instead of permitting), we suggest that smartlets can now be systematically downscaled following Wright's law (*64, 65*), which describes the exponential improvement of technology with cumulative production. The preconditions for such scaling are twofold: the absence of fundamental physical barriers to complex optimization and the capacity for fabricating and testing exponentially growing numbers of modules over time. Now, scaling begins from 2-inch (5.08-cm) wafers producing 64 smartlets of 1-mm size, with the next pipelined step targeting 500-μm smartlets on 4-inch (10.16-cm) wafers, yielding up to 1024 units per wafer. Furthermore, CMOS chiplet fabrication already achieves yields exceeding 100,000 chiplets per 8-inch (20.32-cm) wafer, providing a robust foundation for scalable production. The collective functionalities demonstrated here—including individually controlled locomotion, self-assembly, and advanced intercommunication—reveal the full potential of smartlets as modular microrobots. When considering scaling of communication, locomotion, assembly, and energy harvesting, no insurmountable physical barriers are identified for miniaturization from 1 mm to 20 μm, the scale of biological cells. For instance, although solar power availability decreases with surface area, so do the power requirements of the system. The chiplet controllers now used can easily fit on 250-μm-scale smartlets, with resting power consumption below 2 nW, and can be further scaled to 25 to 50 μm with subnanowatt power consumption using existing 12- to 22-nm CMOS nodes. Tenfold increases in solar harvesting efficiency, achievable through integration of transistor diodes with serial solar cells and optimization of materials, would allow the generation of ~28 nW of solar power on a 20-μm smartlet, sufficient to power its essential operations. However, as shown in our analysis, actuator power demand—particularly for electrolysis-based propulsion—scales subquadratically below a certain critical size, eventually leading to a power mismatch with solar harvesting. μ-LEDs for local communication will face similar issues when scaled to sizes <100 μm. A more detailed assessment of scalability, considering the separate demands on functionality, energy harvesting, locomotion and propulsion, communication, docking, and CMOS control, is included in fig. S12 and the Supplementary Methods: Functional influence of scaling down.

The modular approach opens the path to million-fold fabrication and testing and enables regular halving in size of modules. The integration of active information with smart particles has broad applications from minimally invasive medicine to information-optimized recycling of docked products. The design of the smartlets ensures that all integrated components—solar cells, microchips, actuators, and sensors—are mutually compatible within a highly complex 60+-step fabrication process, enabling mass production at a level of integration previously unattainable for microscale robotic systems. This ensures that our platform not only is functional at the laboratory scale but also paves the way for large-scale manufacturing and real-world applications in areas such as environmental monitoring, targeted drug delivery, and autonomous swarm robotics (*16*).

MATERIALS AND METHODS

Fabrication of light-sensitive structures: μ-OSC and μ-OPD

The fabrication of μ-OSCs and μ-OPDs on a polymeric platform was conducted through a streamlined process where both devices were simultaneously fabricated, sharing several essential elements (see figs. S13 to S15). Analysis regarding morphology, energy band-gap alignment diagram, and material characteristics are provided in figs. S16 and S17.

Bottom contact pattern

The process began with maskless photolithography using AZ 5214 E photoresist (MicroChemicals) to define the electrode structure. The photoresist was spin-coated at 4500 rpm for 45 s to attain 1-μm thickness, soft-baked at 90°C for 4 min, and exposed to UV (365 nm, 15 mW/cm^2) for 5 s. After exposure, samples were baked at 120°C for 2 m, underwent full UV exposure for 30 s, and developed in the AZ 726 MIF developer (MicroChemicals) for 45 s. Ten-nanometer-thick and 50-nm-thick chromium (Cr) and Au films, respectively, were sequentially deposited onto the patterned substrate at a controlled rate of 0.5 Å/s using an electron beam evaporator (Creative Vakuumbeschichtung GmbH). A lift-off process was used thereafter to remove nonexposed photoresist and residual metal layers, yielding a cleanly patterned bottom contact layer crucial for the integration and operation of μ-OSCs and μ-OPDs.

ITO cathode

Preparation for subsequent processing included negative lithography using the AZ 5214 E photoresist onto the electrode contact layer. A 100-nm layer of indium tin oxide (ITO, EvoChem) was then deposited at 0.2 Å/s using a magnetron sputtering machine (Moorfield). After ITO deposition, a lift-off process removed photoresist and any residual metal layers using a mixture of acetone and isopropyl alcohol (Sigma-Aldrich). The samples were annealed at 200°C

Downloaded from https://www.science.org at The Hong Kong University of Science and Technology (Guangzhou) on May 25, 2026

for 5 hours to stabilize the ITO layer and enhance its conductivity, thereby improving the efficiency of μ-OSCs and μ-OPDs.

Electron transport layer

Zinc oxide (ZnO) serves as the ETL, deposited by thermal atomic layer deposition (S100 from Savanna). The process used dimethyl zinc (DMZ) as the precursor and water (H_2O) as the oxidizing agent at a substrate temperature of 200°C. Deposition was carried out at a rate of 30 Å per cycle. Positive lithography was subsequently used to pattern the ZnO layer, which was then etched with an 85% concentration in a volume of phosphoric acid (H_3PO_4, MicroChemicals). A postdeposition annealing at 100°C for 20 min enhanced the electrical and structural properties of the ZnO layer.

Photoactive layer, hole transport, and anode layer

The photoactive material composed of a blend (in 1:1 ratio) of P3HT: $PC_{61}BM$ (Sigma-Aldrich) was dissolved in 1,2-dichlorobenzene (Sigma-Aldrich) at a 20 mg/ml concentration. The solution was spin-coated at 800 rpm for 90 s through a 0.2-μm polytetrafluoroethylene (PTFE) filter and baked at 140°C for 10 min to form a 200-nm-thick film. Methanol immersion for 10 min after spin improved film morphology. The HTL made from poly(3,4-ethylenedioxythiophene) polystyrene sulfonate (PEDOT:PSS, CLEVIOS F HC Solar) was processed by spin-coating a filtered solution at 5000 rpm for 60 s, achieving a thickness of about 50 nm. Annealing at 120°C for 10 min enhanced electrical conductivity and film uniformity. All procedures were conducted in a nitrogen-filled glove box to maintain material integrity. The top electrode was fabricated by depositing a 120-nm layer of Au at a rate of 0.4 Å/s using an electron beam evaporator (Creavac), followed by patterning through positive lithography. Au layer etching with a commercial Au-etching solution (MicroChemicals) and O_2 plasma etching (TEPLA) at 400 W for 5 min defined the device architecture. A lift-off process removed nonexposed photoresist.

Passivation

To protect the devices from the highly basic rolling solution, a protective layer of SU8-2 photoresist (Micro Resist Technology) ~1 μm thick was applied. Spin-coating the photoresist filtered with a 0.2-μm PTFE filter at 8000 rpm for 60 s ensured uniformity. Soft baking at 60°C for 10 min solidified the photoresist, followed by UV exposure (365 nm, 15 mW/cm^2) for 65 s through a photomask. Postexposure baking at 60°C for 5 min further cured and stabilized the photoresist pattern. Development in mr-Dev 600 (Micro Resist Technology) for 60 s removed unexposed photoresist areas, revealing underlying material while preserving the exposed, cross-linked photoresist as a passivation layer.

Structural characterization and analysis

Layer thickness and surface analysis

The thickness of individual layers was accurately measured using a surface profiler (Veeco Dektak 8). Morphological and surface feature assessments were conducted using optical microscopy (Olympus BX5) and scanning electron microscopy (SEM) with a GAIA3 TESCAN operating at an acceleration voltage of 5 kV Ga^+.

Electrical and photovoltaic characterization

The current-voltage (*I-V*) characteristics of the devices were evaluated under a standard intensity of 100 mW/cm^2 using a solar simulator (LSE341, LOT QuantumDesign GmbH) equipped with 150- to 600-W arc lamps. The simulated illumination intensity was calibrated using a commercial optometer (ILT2400, International Light Technologies). *I-V* curves were analyzed using a source meter (Keithley 2636A) across a voltage range of −1 to 1 V for single cells and extended to 3 and 5 V for serially connected cells. Key parameters, including I_{sc}, V_{oc}, maximum power (P_{max}), fill factor (FF), and PCE, were derived from the *I-V* curve [see fig. S18 and Supplementary Methods: Current-voltage (I-V) curve characterization].

Reliability and stability characterization

Planar and tubular μ-OSCs were measured for three different devices to confirm the stable fabrication protocols and performance reliability, as shown in figs. S19 and S20. The operational stability of both planar and tubular μ-OSCs was evaluated over extended periods under ambient conditions to ascertain their long-term reliability and sustainability. Throughout a 31-day testing period, tubular μ-OSCs exhibited excellent stability, retaining up to 60% of their initial PCE and maintaining nearly constant V_{oc}, while directly exposed to atmospheric conditions. In addition, planar μ-OSCs demonstrated retention of 90% under the same conditions (see figs. S21 and S22).

Optical characterization

Angle-dependent performance at varying light incidence angles was assessed (see fig. S23) using an angle-changeable microscope (Keyence VH-Z 100R). The performance of the planar μ-OSCs exhibited systematic variations in response to changing incident angles, as depicted in fig. S24. When the incident light was perpendicular to the device surface, maximizing light absorption, the μ-OSC demonstrated peak performance. In contrast, tubular μ-OSCs responded differently to varying incident angles because of their unique 3D architecture, which facilitated efficient light trapping and absorption from multiple directions. Light illuminating the sides of the tubes can still be effectively absorbed and converted into electrical energy, as shown in fig. S25. This angular versatility inherently enhanced the overall efficiency of μ-OSCs across a wide range of incident angles.

Environmental conditions

All measurements were conducted under ambient conditions to ensure that the data reflected the typical operational environments for these devices.

Fabrication of the self-assembling polymeric platform

The self-assembling polymeric platform provided the foundational structure essential for creating tubular μ-OSCs and 3D micro-origami cubes. The process began by patterning the self-assembling polymer stack as a planar structure, followed by the initiation of rolling and folding mechanisms by the selective release of SLs.

Patterning the self-assembling polymer stack

This procedure was adapted from (*22*). Initially, a glass substrate was treated with oxygen plasma (TEPLA) at 400 W for 2 min to enhance adhesion for the subsequent polymer layers. A lanthanum–acrylic acid–based organometallic photopatternable material was then spin-coated at 3000 rpm for 90 s, soft-baked at 40°C for 10 min, exposed to UV using a MA6 mask aligner (Süss, 365 nm, 15 mW/cm^2) for 60 s, developed in deionized (DI) water for 10 s, and hard-baked at 220°C for 30 min, creating an SL 300 nm thick. A photopatternable hydrogel layer (HGL), serving as the hinge for the origami cube and a rolling platform for tubular μ-OSCs, was then spin-coated at 6000 rpm for 90 s, soft-baked at 40°C for 10 min, exposed to UV using a MA6 mask aligner (Süss, 365 nm, 15 mW/cm^2) for 90 s, developed in diethylene glycol monoethyl ether (Sigma-Aldrich) for

Downloaded from https://www.science.org at The Hong Kong University of Science and Technology (Guangzhou) on May 25, 2026

20 s, and hard-baked at 220°C for 30 min to achieve a thickness of 800 nm. A photopatternable polyimide rigid layer was subsequently applied by spin-coating at 5000 rpm for 90 s, soft-baked at 50°C for 10 min, exposed to UV using a MA6 mask aligner (Süss, 365 nm, 15 mW/cm^2) for 70 s, developed in a mixture of 1 wt % ethanol:2 wt % diethylene glycol monoethyl ether:4 wt % 1-ethyl-2-pyrrolidinon (Sigma-Aldrich) for 60 s, and hard-baked at 220°C for 30 min to reach a thickness of 500 nm. A final, thick layer of 10-μm SU8-25 (Micro Resist Technology) was spin-coated at 3000 rpm for 60 s, soft-baked at 95°C for 4 min, exposed to UV for 80 s, baked at 95°C for 2 min, and developed in mr-Dev 600 for 60 s to be patterned into a square shape. This square structure formed the base of the cube and provided robust support during the folding and manipulation processes (see fig. S26). After the formation of the polymeric platform, μ-OSCs were fabricated as described earlier in Materials and Methods and as shown in fig. S27.

Micro-origami self-assembly process

The self-assembly into both tubes and a cube was initiated by preparing a 0.1 M solution of sodium diethylenetriamine pentaacetic acid (DTPA; Sigma-Aldrich). The pH of the solution was carefully adjusted from 6 to 9 using sodium hydroxide (NaOH; Sigma-Aldrich), a crucial step for controlling the etching rate and selectivity during the removal of the SL. This adjustment influenced the precision of the rolling and folding processes. Once self-assembly was complete, the self-rolled and folded device was immersed in DI water for 20 min to eliminate any residual rolling in solution. Gentle agitation during the washing ensured the cleanliness and structural integrity of the device, preparing it for further processing and evaluation. After micro-origami, the smartlets were stored in medical saline or PBS to preserve their structural integrity.

Analysis of smartlet-integrated μ-OSCs and μ-OPDs

Electrical and photovoltaic characterization

The smartlet-integrated μ-OSCs connected in series were analyzed by recording *I-V* curves. Initially, the devices were evaluated before rolling and folding, with measurements taken across three different devices, as shown in fig. S28. These devices demonstrated maximum efficiency when the incident light angle was perpendicular to the cell. However, when the μ-OSCs were integrated into the smartlet, only the tubular μ-OSCs positioned at the top could efficiently absorb light, leading to a V_{oc} of 2.1 to 3.1 V instead of 5.2 V, as illustrated in fig. S9.

Omnidirectional photovoltaic analysis

To characterize the omnidirectional light-harvesting capability of the fully assembled cube, we designed a 3D-printed (SLA 3D printer from Formlabs) hollow hemisphere and placed 16 NeoPixel LED strips along the azimuthal axis, resulting in an angular distribution of one LED for every 22.5°. Each of the 16 LED strips consisted of ~21 LEDs distributed along the altitude axis, resulting in an angular distribution of one LED for every 17.5°. All LEDs were calibrated to output 50 μW/cm^2 with the projection aimed at the center of the hemisphere. This setup is shown in fig. S29 and has been used in the experiments corresponding to Fig. 2 (A to F) and figs. S6 to S8. This configuration ensured uniform light distribution from multiple directions, where the LEDs were programmed and controlled to operate at arbitrary positions. To assess the individual solar cell performance on the basis of their position within the smartlet, we separately contacted each cell (see fig. S6). Figures S7 and S8 demonstrated that, when the incident light is directly or closely aligned with a particular μ-OSC, it exhibits dominant energy harvesting compared with μ-OSCs positioned farther away from the light source. This positional dependence highlights the importance of spatial arrangement and orientation optimization for maximizing energy absorption and overall device performance. Movie S8 shows the real-time positional and orientational measurements of a smartlet.

Preparation for SLID bonding

Although conductive epoxy-based transfer bonding methods are well documented (*66*), we demonstrated an alternative approach by extending the solid-liquid interdiffusion (SLID) bonding technique to ultrathin polymeric films (thickness less than 5 μm). The Cu- and Sn-based SLID bonding method reduces resistance compared with traditional epoxy-based transfer bonding techniques, offering a substantial improvement in electrical performance.

For the preparation of the SLID bonding, which is crucial for integrating μ-LEDs and μ-chips, Cu and Sn were selected as conductive and solder materials because of their established properties in bonding applications. Cu and Sn layers were deposited using a standard electroplating technique, achieving thicknesses of 10 and 5 μm, respectively. After deposition, a reflow process was carried out under vacuum conditions to form well-defined solder bumps, thereby enhancing bonding efficiency (see fig. S30). The alignment and bonding of flipped chips were performed using a commercial bonding machine (FinePlacer Pico), adhering to precise pressure and temperature profiles to ensure reliable and precise connections between components. This was critical for the functionality and performance of the integrated devices. The adaptation of advanced SLID bonding technology to polymeric thin-film substrates facilitated the reliable bonding of both custom CMOS chiplets—nW-powered 140 μm–by–140 μm–by–35 μm microcontrollers with 12 or more pins—and simpler chiplets, including micro-LED chips (see figs. S31 and S32). The sequential bonding process of the μ-chip and μ-LEDs is described in fig. S33 and movie S9.

Lablet μ-chips

The description and programming of the custom lablet μ-chip1 and commercial LED driver μ-chip2 are described in Supplementary Methods: Description of lablet μChips, Programming of lablet μ-Chips, Description of the commercial LED driver chiplet, and Programming of LED driver μ-Chips and tables S2 to S4. The short summary of lablets here gives readers the necessary orientation on their nature and use. Lablets were thinned and singulated from combinatorial variant array chips (each containing ~1000 lablets) designed at the Ruhr Universität Bochum and fabricated at wafer scale at Taiwan Semiconductor Manufacturing Company (TSMC) in a 180-nm CMOS (*13*). The 58-bit program for the lablets is serially loaded in a shift register and species details and timing for four phases of processing, as temporal patterns of tristate or active signals on specific subsets of the three dedicated and three facultative actuator electrodes, as well as conditional switching between the phases dependent on digital signals derived from the two electrochemical sensors. Other features of the programmable finite state machine, including the ability to record sensor data and to replicate itself between lablets, were not used in the current work. Detailed operation frequency and output current are discussed in fig. S34.

Downloaded from https://www.science.org at The Hong Kong University of Science and Technology (Guangzhou) on May 25, 2026

Operation of μ-LEDs

Detailed operational description of the green and red μ-LEDs is discussed in Supplementary Methods: Detailed description of μ-LED chips and tables S5 and S6, including emission characteristics, voltage requirement, and spectral properties. After the SLID bonding process, successful bonding was confirmed through the illumination of μ-LEDs, demonstrating their functionality even with different color combinations, as shown in fig. S35.

Fabrication of BGEs

The complete fabrication of a smartlet began with the creation of the polymeric origami platform, followed by BGEs, μ-OSC and μ-OPD layer deposition and patterning, SLID bonding of μ-LEDs and a μ-chip, and last, SU-8 photoresist passivation.

Oxygen evolution reaction

To facilitate the oxygen evolution reaction, a thin layer of Ni, recognized for its photocatalytic properties, was deposited. The Ni layer was precisely patterned using negative lithography and deposited through magnetron sputtering at a controlled rate of 0.5 Å/s to achieve a thickness of 15 nm. After deposition, a lift-off process using acetone and isopropanol was conducted to remove excess material and accurately define the desired pattern.

Hydrogen evolution reaction

For the hydrogen evolution reaction, Pt was used as the primary catalyst. Similar to the Ni deposition, negative lithography was used to ensure the precise placement of the Pt layer. Before depositing Pt, a Ti layer was applied using an electron beam evaporator (Creavac) to serve as an adhesive layer. The deposition rates for Ti and Pt were 0.2 Å/s, resulting in thicknesses of 5 and 10 nm, respectively. A lift-off process in acetone and isopropanol followed to remove any residual metal, thereby defining the clean and precise pattern required for effective catalytic activity. Note that DI water was unsuitable for efficient electrolysis because of its high impedance, resulting in minimal or no gas generation (*52*), which would negatively affect propulsion.

Fabrication of the hydrophobic layer for patterned smartlet docking control

This procedure was only used for the customization of smartlet cube exterior faces for specific docking, as shown in Fig. 5. The preparation of the hydrophobic layer began with AZ5214E negative lithography (details described above) on the SL to pattern areas corresponding to the faces of the smartlet, followed by a 200-nm-thick amorphous MoO_3 grown by electron beam deposition (Edwards) at a rate of 0.2 Å/s. Then, a lift-off process was performed in acetone and isopropanol. This pattern served as a water-soluble SL for patterning the hydrophobic material (ETC-PRO, from EVOCHEM), which was deposited to a thickness of 100 nm using electron beam evaporation (Edwards). Given the good solubility of MoO_3 in H_2O, the hydrophobic materials were lifted off in DI water. As a result, the hydrophobic material that was not deposited onto the MoO_3 layer remained on the substrate, forming a well-defined pattern. At the end of the fabrication sequence, a curing step was performed by heating the samples to 170°C for 2 hours to ensure the activation of the hydrophobic material. A detailed analysis of the strength of hydrophobic and hydrophilic interactions driving self-assembly, along with their sufficiency in supporting the intended movements in water and at the water-air interface, is discussed in Supplementary Methods: Detailed calculation of hydrophobic and hydrophilic interactions in self-assembly and motion at interfaces and table S1.

Experimental setup for controlled locomotion and self-assembly

The measurement setup to operate the fully equipped smartlets is illustrated in fig. S36. It consisted of a solar simulator to provide a 1-sun calibrated light source and an LED light source at the top of the beaker as a global programming source. Note that this was in addition to the onboard LEDs used for smartlet peer-to-peer communication (see Fig. 3, F and G), including messaging commands and (re)programming. A logic analyzer for programming the chiplets (digital discovery logic analyzer) and two cameras (cam1: Basler acA1300-200uc; cam2: Keyence VHX digital camera) at different angles to capture the locomotion process from multiple perspectives were also part of the setup. Smartlets were immersed in a 60-ml beaker filled with water (see below) and 0.075% methylene blue to accelerate the dissolution of O_2 and H_2 bubbles at the water-air interface. DI water was not used for propulsion because of its low ion concentration and conductivity, which hinders the electrolysis process, resulting in minimal or no gas generation (*57*). In addition, DI water is highly susceptible to pH fluctuations because of the absence of buffering ions, making electrolysis performance variable. In contrast, both medical saline and filtered lake water exhibited greater pH stability because of the presence of dissolved salts and natural buffering agents, ensuring more consistent electrochemical performance for sustained propulsion. To ensure experimental consistency and to evaluate propulsion robustness across different environments, we first tested all smartlets in medical saline as a reference medium before conducting experiments in filtered lake water. Medical saline was selected because its ionic composition closely mimics physiological conditions, making it relevant for biomedical applications. In contrast, filtered lake water represents an ecologically relevant environment where the smartlets could operate effectively. The hydrophobic-hydrophilic docking experiments were conducted in real-world relevant aqueous fluids, specifically medical saline and filtered lake water, to assess the system's robustness under different environmental conditions. The lake water, sourced from the nearby castle pond (with a typical European fresh water lake chemical composition as presented in Supplementary Methods: Detailed description of aqueous fluids and table S7), underwent sequential filtration using polyvinylidene difluoride (PVDF) filters with progressively smaller pore sizes (100 μm → 50 μm → 10 μm → 5 μm → 1 μm), ensuring the removal of larger particulates while retaining its natural ionic and small-molecule (natural surfactant) composition.

Statistical analysis

All quantitative measurements—including power generation, buoyancy cycling times, and communication response rates—are reported as mean values with error bars representing the SD, unless stated otherwise. For each metric, measurements were obtained from three independently fabricated devices with five repeated trials per condition ($n = 5$). No statistical methods were used to predetermine sample size, and no data were excluded from analysis. Statistical significance testing was not applied because the goal was to assess functional consistency and reliability rather than hypothesis testing.

Downloaded from https://www.science.org at The Hong Kong University of Science and Technology (Guangzhou) on May 25, 2026

Supplementary Materials

The PDF file includes:
Figs. S1 to S36
Supplementary Methods
Tables S1 to S7
References (*67*–*92*)

Other Supplementary Material for this manuscript includes the following:
Movies S1 to S9

REFERENCES AND NOTES

1. D. Murat, M. Byrne, A. Komeili, Cell biology of prokaryotic organelles. *Cold Spring Harb. Perspect. Biol.* **2**, a000422 (2010).
2. M. F. Reynolds, A. J. Cortese, Q. Liu, Z. Zheng, W. Wang, S. L. Norris, S. Lee, M. Z. Miskin, A. C. Molnar, I. Cohen, P. L. McEuen, Microscopic robots with onboard digital control. *Sci. Robot.* **7**, eabq2296 (2022).
3. V. K. Bandari, Y. Nan, D. Karnaushenko, Y. Hong, B. Sun, F. Striggow, D. D. Karnaushenko, C. Becker, M. Faghih, M. Medina-Sánchez, F. Zhu, O. G. Schmidt, A flexible microsystem capable of controlled motion and actuation by wireless power transfer. *Nat. Electron.* **3**, 172–180 (2020).
4. E. Bray, R. Groß, Recent developments in self-assembling multi-robot systems. *Curr. Robot. Rep.* **4**, 101–116 (2023).
5. Q. He, R. Yin, Y. Hua, W. Jiao, C. Mo, H. Shu, J. R. Raney, A modular strategy for distributed, embodied control of electronics-free soft robots. *Sci. Adv.* **9**, eade9247 (2023).
6. W. Haouas, M. Gauthier, K. Rabenorosoa, Miniaturized soft robotics: Recent advances and future opportunities. *Curr. Robot. Rep.* **5**, 15–27 (2024).
7. M. Ye, Y. Zhou, H. Zhao, Z. Wang, B. J. Nelson, X. Wang, A review of soft microrobots: Material, fabrication, and actuation. *Adv. Intell. Syst.* **5**, 2300311 (2023).
8. S. S. Iyer, B. Vaisband, "Heterogeneous integration at scale" in *Advances in Semiconductor Technologies* (Wiley, 2022), pp. 1–24.
9. K. Rogdakis, G. Psaltakis, G. Fagas, A. Quinn, R. Martins, E. Kymakis, Hybrid chips to enable a sustainable internet of things technology: Opportunities and challenges. *Discov. Mater.* **4**, 00074 (2024).
10. C. S. Bick, I. Lee, T. Coote, A. E. Haponski, D. Blaauw, D. Ó. Foighil, Millimeter-sized smart sensors reveal that a solar refuge protects tree snail *Partula hyalina* from extirpation. *Commun. Biol.* **4**, 744 (2021).
11. S. Carrara, Body dust: Well beyond wearable and implantable sensors. *IEEE Sens. J.* **21**, 12398–12406 (2021).
12. D. A. Funke, P. Hillger, J. Oehm, P. Mayr, L. Straczek, N. Pohl, J. S. McCaskill, A 200 µm by 100 µm smart submersible system with an average current consumption of 1.3 nA and a compatible voltage converter. *IEEE Trans. Circuits Syst. I Regul. Pap.* **64**, 3013–3024 (2017).
13. T. Maeke, J. S. Matsarskaia, D. Funke, P. Mayr, A. Sharma, U. Tangen, J. Oehm, Autonomous programmable microscopic electronic lablets optimized with digital control. arXiv:2405.20110 [cs.RO] (2024).
14. Y. Mei, A. A. Solovev, S. Sanchez, O. G. Schmidt, Rolled-up nanotech on polymers: From basic perception to self-propelled catalytic microengines. *Chem. Soc. Rev.* **40**, 2109–2119 (2011).
15. H. J. Levinson, High-NA EUV lithography: Current status and outlook for the future. *Jpn. J. Appl. Phys.* **61**, 1347–4065 (2022).
16. J. S. McCaskill, D. Karnaushenko, M. Zhu, O. G. Schmidt, Microelectronic morphogenesis: Smart materials with electronics assembling into artificial organisms. *Adv. Mater.* **35**, e2306344 (2023).
17. B. Warneke, M. Last, B. Liebowitz, K. S. J. Pister, Smart dust: Communicating with a cubic-millimeter computer. *Computertomographie* **34**, 44–51 (2001).
18. D. Seo, R. M. Neely, K. Shen, U. Singhal, E. Alon, J. M. Rabaey, J. M. Carmena, M. M. Maharbiz, Wireless recording in the peripheral nervous system with ultrasonic neural dust. *Neuron* **91**, 529–539 (2016).
19. V. Iyer, H. Gaensbauer, T. L. Daniel, S. Gollakota, Wind dispersal of battery-free wireless devices. *Nature* **603**, 427–433 (2022).
20. J. S. McCaskill, T. Maeke, D. Funke, P. Mayr, A. Sharma, P. F. Wagler, J. Oehm, Design and fabrication of autonomous electronic lablets for chemical control. arXiv:2405.15608 [cs. RO] (2024).
21. S. Chen, J. Chen, X. Zhang, Z.-Y. Li, J. Li, Kirigami/origami: Unfolding the new regime of advanced 3D microfabrication/nanofabrication with "folding". *Light Sci. Appl.* **9**, 75 (2020).
22. D. Karnaushenko, N. Münzenrieder, D. D. Karnaushenko, B. Koch, A. K. Meyer, S. Baunack, L. Petti, G. Tröster, D. Makarov, O. G. Schmidt, Biomimetic microelectronics for regenerative neuronal cuff implants. *Adv. Mater.* **27**, 6797–6805 (2015).
23. C. Becker, B. Bao, D. D. Karnaushenko, V. K. Bandari, B. Rivkin, Z. Li, M. Faghih, D. Karnaushenko, O. G. Schmidt, A new dimension for magnetosensitive e-skins: Active matrix integrated micro-origami sensor arrays. *Nat. Commun.* **13**, 2121 (2022).
24. E. Smela, O. Inganäs, I. Lundström, Controlled folding of micrometer-size structures. *Science* **268**, 1735–1738 (1995).
25. Z. Lin, L. S. Novelino, H. Wei, N. A. Alderete, G. H. Paulino, H. D. Espinosa, S. Krishnaswamy, Folding at the microscale: Enabling multifunctional 3D origami-architected metamaterials. *Small* **16**, e2002229 (2020).
26. L. Merces, L. M. M. Ferro, A. Thomas, D. D. Karnaushenko, Y. Luo, A. I. Egunov, W. Zhang, V. K. Bandari, Y. Lee, J. S. McCaskill, M. Zhu, O. G. Schmidt, D. Karnaushenko, Bio-inspired dynamically morphing microelectronics toward high-density energy applications and intelligent biomedical implants. *Adv. Mater.* **36**, e2313327 (2024).
27. E. Gultepe, J. S. Randhawa, S. Kadam, S. Yamanaka, F. M. Selaru, E. J. Shin, A. N. Kalloo, D. H. Gracias, Biopsy with thermally-responsive untethered microtools. *Adv. Mater.* **25**, 514–519 (2013).
28. W. Wang, Q. Liu, I. Tanasijevic, M. F. Reynolds, A. J. Cortese, M. Z. Miskin, M. C. Cao, D. A. Muller, A. C. Molnar, E. Lauga, P. L. McEuen, I. Cohen, Cilia metasurfaces for electronically programmable microfluidic manipulation. *Nature* **605**, 681–686 (2022).
29. T. Xiao-qing, Z. Shuai, Y. Yang, Z. Shu-ling, W. Xiao-chuan, "Micro-scale RF energy harvesting and power management for passive IoT devices" in *2019 IEEE 2nd International Conference on Renewable Energy and Power Engineering (REPE)* (IEEE, 2019), pp. 54–58.
30. A. J. Cortese, C. L. Smart, T. Wang, M. F. Reynolds, S. L. Norris, Y. Ji, S. Lee, A. Mok, C. Wu, F. Xia, N. I. Ellis, A. C. Molnar, C. Xu, P. L. McEuen, Microscopic sensors using optical wireless integrated circuits. *Proc. Natl. Acad. Sci. U.S.A.* **117**, 9173–9179 (2020).
31. L. Zhang, W. Du, J.-H. Kim, C.-C. Yu, C. Dagdeviren, An emerging era: Conformable ultrasound electronics. *Adv. Mater.* **36**, e2307664 (2024).
32. M. F. Reynolds, M. Z. Miskin, Materials for electronically controllable microactuators. *MRS Bull.* **49**, 107–114 (2024).
33. C.-Y. You, B.-F. Hu, B.-R. Xu, Z.-Y. Zhang, B.-M. Wu, G.-S. Huang, E.-M. Song, Y.-F. Mei, Foldable-circuit-enabled miniaturized multifunctional sensor for smart digital dust. *Chip* **1**, 100034 (2022).
34. J. Biggs, J. Myers, J. Kufel, E. Ozer, S. Craske, A. Sou, C. Ramsdale, K. Williamson, R. Price, S. White, A natively flexible 32-bit Arm microprocessor. *Nature* **595**, 532–536 (2021).
35. V. K. Bandari, O. G. Schmidt, System-engineered miniaturized robots: From structure to intelligence. *Adv. Intell. Syst.* **3**, 2000284 (2021).
36. P. McLellan, "How to make chiplets a viable market," *Cadence Blogs*, 8 February 2023; https://community.cadence.com/cadence_blogs_8/b/breakfast-bytes/posts/how-to-make-chiplets-a-viable-market.
37. P. Vijay, V. Sumaria, "Advancement in P3HT PCBM solar cells, the most efficient polymer photovoltaic cell" in *10th Annual Session of Students' Chemical Engineering Congress (SCHEMCON)* (Indian Institute of Chemical Engineers, 2014), pp. 1–14.
38. Worldsemi, WS2812B intelligent control LED integrated light source; http://world-semi.com/ws2812-family/.
39. R. Xu, Q. Xu, A survey of recent developments in magnetic microrobots for micro-/nano-manipulation. *Micromachines* **15**, 468 (2024).
40. Y. Zheng, H. Zhao, Y. Cai, B. Jurado-Sánchez, R. Dong, Recent advances in one-dimensional micro/nanomotors: Fabrication, propulsion and application. *Nanomicro Lett.* **15**, 20 (2023).
41. A. K. Shukla, S. Bhandari, S. Mitra, B. Kim, K. K. Dey, Buoyancy-driven micro/-nanomotors: From fundamentals to applications. *Small* **20**, e2308580 (2024).
42. G. Gardi, S. Ceron, W. Wang, K. Petersen, M. Sitti, Microrobot collectives with reconfigurable morphologies, behaviors, and functions. *Nat. Commun.* **13**, 2239 (2022).
43. A. Abdel-Rahman, C. Cameron, B. Jenett, M. Smith, N. Gershenfeld, Self-replicating hierarchical modular robotic swarms. *Commun. Eng.* **1**, 35 (2022).
44. P. W. K. Rothemund, Using lateral capillary forces to compute by self-assembly. *Proc. Natl. Acad. Sci. U.S.A.* **97**, 984–989 (2000).
45. N. Bowden, A. Terfort, J. Carbeck, G. M. Whitesides, Self-assembly of mesoscale objects into ordered two-dimensional arrays. *Science* **276**, 233–235 (1997).
46. R. Niu, C. X. Du, E. Esposito, J. Ng, M. P. Brenner, P. L. McEuen, I. Cohen, Magnetic handshake materials as a scale-invariant platform for programmed self-assembly. *Proc. Natl. Acad. Sci. U.S.A.* **116**, 24402–24407 (2019).
47. V. A. Sontakke, Y. Yokobayashi, Programmable macroscopic self-assembly of DNA-decorated hydrogels. *J. Am. Chem. Soc.* **144**, 2149–2155 (2022).
48. C. Chen, S. Ding, J. Wang, Materials consideration for the design, fabrication and operation of microscale robots. *Nat. Rev. Mater.* **9**, 159–172 (2024).
49. E. Petritoli, F. Leccese, M. Cagnetti, High accuracy buoyancy for underwater gliders: The uncertainty in the depth control. *Sensors* **19**, 1831 (2019).
50. A. Sharma, J. S. McCaskill, "Autonomous lablet locomotion and active docking by sensomotory electroosmotic drive" in *Proceedings of the ECAL 2015: The 13th European Conference on Artificial Life* (International Society for Artificial Life, 2015), pp. 456–462.
51. O. Matsarskaia, F. Roosen-Runge, F. Schreiber, Multivalent ions and biomolecules: Attempting a comprehensive perspective. *ChemPhysChem* **21**, 1742–1767 (2020).
52. J. Dziadkowiec, M. Ban, S. Javadi, B. Jamtveit, A. Røyne, Ca^{2+} ions decrease adhesion between two (104) calcite surfaces as probed by atomic force microscopy. *ACS Earth Space Chem.* **5**, 2827–2838 (2021).

Downloaded from https://www.science.org at The Hong Kong University of Science and Technology (Guangzhou) on May 25, 2026

53. E. Duboué-Dijon, P. Delcroix, H. Martinez-Seara, J. Hladílková, P. Coufal, T. Křížek, P. Jungwirth, Binding of divalent cations to insulin: Capillary electrophoresis and molecular simulations. *J. Phys. Chem. B* **122**, 5640–5648 (2018).
54. F. Dawson, W. C. Yew, B. Orme, C. Markwell, R. Ledesma-Aguilar, J. J. Perry, I. M. Shortman, D. Smith, H. Torun, G. Wells, M. G. Unthank, Self-assembled, hierarchical structured surfaces for applications in (super)hydrophobic antiviral coatings. *Langmuir* **38**, 10632–10641 (2022).
55. F. Staniscia, H. V. Guzman, M. Kanduč, Tuning contact angles of aqueous droplets on hydrophilic and hydrophobic surfaces by surfactants. *J. Phys. Chem. B* **126**, 3374–3384 (2022).
56. B. Mewafy, F. Paloukis, K. M. Papazisi, S. P. Balomenou, W. Luo, D. Teschner, O. Joubert, A. L. G. L. Salle, D. K. Niakolas, S. Zafeiratos, Influence of surface state on the electrochemical performance of nickel-based cermet electrodes during steam electrolysis. *ACS Appl. Energy Mater.* **2**, 7045–7055 (2019).
57. H. Becker, J. Murawski, D. V. Shinde, I. E. L. Stephens, G. Hinds, G. Smith, Impact of impurities on water electrolysis: A review. *Sustain. Energy Fuels* **7**, 1565–1603 (2023).
58. J. Lee, Y. Yoon, H. Park, J. Choi, Y. Jung, S. H. Ko, W.-H. Yeo, Bioinspired soft robotic fish for wireless underwater control of gliding locomotion. *Adv. Intell. Syst.* **4**, 2100271 (2022).
59. J. Bang, S. H. Choi, K. R. Pyun, Y. Jung, S. Hong, D. Kim, Y. Lee, D. Won, S. Jeong, W. Shin, S. H. Ko, Bioinspired electronics for intelligent soft robots. *Nat. Rev. Electr. Eng.* **1**, 597–613 (2024).
60. B. J. Nelson, I. K. Kaliakatsos, J. J. Abbott, Microrobots for minimally invasive medicine. *Annu. Rev. Biomed. Eng.* **15**, 55–58 (2010).
61. C. Hu, S. Pané, B. J. Nelson, Soft micro- and nanorobotics. *Annu. Rev. Control Robot. Auton. Syst.* **1**, 53–75 (2018).
62. K. Peyer, L. Zhang, B. Nelson, Bio-inspired magnetic swimming microrobots for biomedical applications. *Nanoscale* **5**, 1259–1272 (2013).
63. M. Medina-Sánchez, V. Magdanz, M. Guix, V. M. Fomin, O. G. Schmidt, Swimming microrobots: Soft, reconfigurable, and smart. *Adv. Funct. Mater.* **28**, 1707228 (2018).
64. B. Nagy, J. D. Farmer, Q. M. Bui, J. E. Trancik, Statistical basis for predicting technological progress. *PLOS ONE* **8**, e52669 (2013).
65. J. D. Farmer, F. Lafond, How predictable is technological progress? *Res. Policy* **45**, 647–665 (2016).
66. H. Yoon, S. Jeong, B. Lee, Y. Hong, A site-selective integration strategy for microdevices on conformable substrates. *Nat. Electron.* **7**, 383–395 (2024).
67. M. V. Mirkin, S. Amemiya, Eds. *Nanoelectrochemistry* (CRC Press, ed. 1, 2015).
68. V. B. Svetovoy, R. G. P. Sanders, M. C. Elwenspoek, Transient nanobubbles in short-time electrolysis. *J. Phys. Condens. Matter* **25**, 184002 (2013).
69. S. S. Veroneau, A. C. Hartnett, J. Ryu, H. Hong, C. Costentin, D. G. Nocera, A straightforward model for quantifying local pH gradients governing the oxygen evolution reaction. *J. Am. Chem. Soc.* **146**, 28925–28931 (2024).
70. T. S. Jacobs, S. Park, M. Schönig, B. M. Weckhuysen, M. T. M. Koper, W. van der Stam, Luminescence thermometry probes local heat effects at the platinum electrode surface during alkaline water electrolysis. *ACS Energy Lett.* **9**, 3335–3341 (2024).
71. J. Qiu, J. Yao, Z. Feng, B. Huang, Z. Luo, L. Wang, Enhancing water electrolysis performance by bubble behavior management. *Small Methods* **2025**, 2402105 (2025).
72. Y. He, Y. Cui, Z. Zhao, Y. Chen, W. Shang, P. Tan, Strategies for bubble removal in electrochemical systems. *Energy Rev.* **2**, 100015 (2023).
73. N. T. T. Thao, J. U. Jang, A. K. Nayak, H. Han, Current trends of iridium-based catalysts for oxygen evolution reaction in acidic water electrolysis. *Small Sci.* **4**, 2300109 (2024).
74. F.-D. Kong, J. Liu, A.-X. Ling, Z.-Q. Xu, M.-J. Shi, Q.-S. Kong, H.-Y. Wang, Overlapping structure of platinum-iridium oxide layers and its electrocatalytic behavior on bifunctional oxygen electrode. *Catal. Commun.* **90**, 19–22 (2017).
75. K. Daems, P. Yadav, K. B. Dermenci, J. Van Mierlo, M. Berecibar, Advances in inorganic, polymer and composite electrolytes: Mechanisms of lithium-ion transport and pathways to enhanced performance. *Renew. Sustain. Energy Rev.* **191**, 114136 (2024).
76. A. Alizadeh, W.-L. Hsu, M. Wang, H. Daiguji, Electroosmotic flow: From microfluidics to nanofluidics. *Electrophoresis* **42**, 834–868 (2021).
77. H. Shigemune, K. Pradidarcheep, Y. Kuwajima, Y. Seki, S. Maeda, V. Cacucciolo, Wireless electrohydrodynamic actuators for propulsion and positioning of miniaturized floating robots. *Adv. Intell. Syst.* **3**, 2100004 (2021).
78. J. Yao, K. Zhao, J. Lou, K. Zhang, Recent advances in dielectrophoretic manipulation and separation of microparticles and biological cells. *Biosensors* **14**, 417 (2024).
79. G. W. Slater, F. Tessier, K. Kopecka, The electroosmotic flow (EOF). *Methods Mol. Biol.* **583**, 121–134 (2010).
80. X. Wang, C. Cheng, S. Wang, S. Liu, Electroosmotic pumps and their applications in microfluidic systems. *Microfluid Nanofluidics* **6**, 145–162 (2009).
81. A. Castellanos, A. Ramos, A. González, N. G. Green, H. Morgan, Electrohydrodynamics and dielectrophoresis in microsystems: Scaling laws. *J. Phys. D Appl. Phys.* **36**, 2584–2597 (2003).
82. D. Karnaushenko, D. D. Karnaushenko, D. Makarov, S. Baunack, R. Schäfer, O. G. Schmidt, Self-assembled on-chip-integrated giant magneto-impedance sensorics. *Adv. Mater.* **27**, 6582–6589 (2015).
83. J. Y. Kim, S. Noh, D. Lee, P. K. Nayak, Y. Hong, C. Lee, Solution-processable zinc oxide for the polymer solar cell based on P3HT:PCBM. *J. Nanosci. Nanotechnol.* **11**, 5995–6000 (2011).
84. P. M. Aneesh, C. R. Kumar, P. C. R. Varma, K. Vivek, M. A. G. Namboothiry, Enhancement in photovoltaic properties of plasmonic nanostructures incorporated organic solar cells processed in air using P3HT:PCBM as a model active layer. *Org. Photonics. Photovolt.* **3**, 64 (2015).
85. M. Thanihaichelvan, K. Sockiah, K. Balashangar, P. Ravirajan, Cadmium sulfide interface layer for improving the performance of titanium dioxide/poly (3-hexylthiophene) solar cells by extending the spectral response. *J. Mater. Sci. Mater. Electron.* **26**, 3558–3563 (2015).
86. J. S. McCaskill, G. Von Kiedrowsk, J. Öhm, P. Mayr, L. Cronin, I. Willner, A. Herrmann, S. Rasmussen, F. Stepanek, N. H. Packard, P. R. Wills, Microscale chemically reactive electronic agents. *Int. J. Unconv. Comput.* **8**, 289–299 (2012).
87. European Environment Agency, "Nutrients in freshwater in Europe" (2024); https://eea.europa.eu/en/analysis/indicators/nutrients-in-freshwater-in-europe.
88. European Environment Agency, "European waters getting cleaner, but big challenges remain" (2018); https://networknature.eu/sites/default/files/images/EEA%20water%20report.pdf.
89. X. Luo, Q. Huo, X. Liu, C. Zheng, Y. Liu, Effect of hydrophilic or hydrophobic interactions on the self-assembly behavior and micro-morphology of a collagen mimetic peptide. *J. Leather Sci. Eng.* **3**, 11 (2021).
90. B. Lindman, B. Medronho, L. Alves, M. Norgren, L. Nordenskiöld, Hydrophobic interactions control the self-assembly of DNA and cellulose. *Q. Rev. Biophys.* **54**, e3 (2021).
91. Y. Cao, D. Wang, P. Zhou, Y. Zhao, Y. Sun, J. Wang, Influence of conventional surfactants on the self-assembly of a bola type amphiphilic peptide. *Langmuir* **33**, 5446–5455 (2017).
92. S. H. Donaldson, C. T. Lee Jr., B. F. Chmelka, J. N. Israelachvili, General hydrophobic interaction potential for surfactant/lipid bilayers from direct force measurements between light-modulated bilayers. *Proc. Natl. Acad. Sci. U.S.A.* **108**, 15699–15704 (2011).

Acknowledgments: J.S.M. wishes to acknowledge especially the contribution of T. Maeke, D. Funke, P. Mayr, and J. Oehm in codesigning the electronics of the lablet μ-chips used in this work. We thank C. N. Saggau for absorption measurements and C. Schmidt, A. M. Placht, A. Dumler, and P. Plocica for technical support and lab maintenance. J. Müller, press office TU Chemnitz, took the photo used in Fig. 1C, and P. Radha produced the animation in movie S1. We discussed the smartlet concept at TU Chemnitz with proposed partners in the Microelectronic Morphogenesis (MIMO) initiative. **Funding:** O.G.S. acknowledges financial support from the European Research Council (ERC) under the European Union's Horizon 2020 research and innovation program (grant agreement no. 835268). O.G.S. and D.K. acknowledge support from the German Research Foundation DFG (SCHM 1298/26-1, SCHM 1298/32-1, and KA5051/3-1). This work was cofinanced by tax revenue on the basis of the budget approved by the members of the Saxony State Parliament. **Author contributions:** Conceptualization: V.K.B., O.G.S., J.S.M., Y.L., and D.K. Methodology: Y.L., V.K.B., and O.G.S. Investigation: Y.L. and V.K.B. Validation: Y.L., V.K.B., and O.G.S. Formal analysis: Y.L., V.K.B., and O.G.S. Resources: J.S.M., D.D.K., and D.K. Data curation: Y.L., V.K.B., and O.G.S. Writing—original draft: Y.L., V.K.B., J.S.M., and O.G.S. Writing—review and editing: Y.L., V.K.B., J.S.M., O.G.S., D.K., and D.D.K. Visualization: Y.L. and V.K.B. Supervision: V.K.B., O.G.S., and J.S.M. Project administration: V.K.B. and O.G.S. Custom chiplets: J.S.M. and O.G.S. conceived the low-power integrating role; J.S.M. provided the CMOS lablets and, with V.K.B., supervised the singulation, programming, and use of the lablet microchips by P.A. and Y.L. The CMOS lablets were created at wafer scale in the EU project no. 318671, conceived and coordinated by J.S.M. Polymeric layer stacks: D.D.K. and D.K. prepared the materials. **Competing interests:** The authors declare that they have no competing interests. **Data and materials availability:** All data needed to evaluate the conclusions in the paper are present in the paper and/or the Supplementary Materials. All of the materials and source codes are available at Zenodo: DOI 10.5281/zenodo.16321684.

Submitted 13 November 2024
Accepted 22 July 2025
Published 20 August 2025
10.1126/scirobotics.adu6007

Downloaded from https://www.science.org at The Hong Kong University of Science and Technology (Guangzhou) on May 25, 2026

Science Robotics

Si chiplet–controlled 3D modular microrobots with smart communication in natural aqueous environments

Yeji Lee, Vineeth K. Bandari, John S. McCaskill, Pranathi Adluri, Daniil Karnaushenko, Dmitriy D. Karnaushenko, and Oliver G. Schmidt

Sci. Robot. **10** (105), eadu6007. DOI: 10.1126/scirobotics.adu6007

View the article online
https://www.science.org/doi/10.1126/scirobotics.adu6007
Permissions
https://www.science.org/help/reprints-and-permissions

Downloaded from https://www.science.org at The Hong Kong University of Science and Technology (Guangzhou) on May 25, 2026

Use of this article is subject to the Terms of service

Science Robotics (ISSN 2470-9476) is published by the American Association for the Advancement of Science. 1200 New York Avenue NW, Washington, DC 20005. The title *Science Robotics* is a registered trademark of AAAS.

Copyright © 2025 The Authors, some rights reserved; exclusive licensee American Association for the Advancement of Science. No claim to original U.S. Government Works